Very preliminary reference Moon model

Raphaël F. Garcia [a,b,*], Jeannine Gagnepain-Beyneix [c], Sébastien Chevrot [a,b], Philippe Lognonné [c]

[a] Université de Toulouse, UPS-OMP, IRAP, Toulouse, France
[b] CNRS, IRAP, 14, Avenue Edouard Belin, F-31400 Toulouse, France
[c] Equipe Géophysique Spatiale et Planétaire, Institut de Physique du Globe, Sorbonne Paris Cité, Univ Paris Diderot, UMR 7154 CNRS, 4 Ave de Neptune, F-94100 Saint Maur des Fossés, France

A B S T R A C T

The deep structure of the Moon is a missing piece to understand the formation and evolution of the Earth–Moon system. Despite the great amount of information brought by the Apollo passive seismic experiment (ALSEP), the lunar structure below deep moonquakes, which occur around 900 km depth, remains largely unknown. We construct a reference Moon model which incorporates physical constraints, and fits both geodesic (lunar mass and polar moment of inertia, and Love numbers) and seismological (body wave arrivals measured by Apollo network) data. In this model, the core radius is constrained by the detection of S waves reflected from the core. In a first step, for each core radius, a radial model of the lunar interior, including P and S wave velocities and density, is inverted from seismic and geodesic data. In a second step, the core radius is determined from the detection of shear waves reflected on the lunar core by waveform stacking of deep moonquake Apollo records. This detection has been made possible by careful data selection and processing, including a correction of the gain of horizontal sensors based on the principle of energy equipartition inside the coda of lunar seismic records, and a precise alignment of SH waveforms by a non-linear inversion method. The Very Preliminary REference MOON model (VPREMOON) obtained here has a core radius of 380 ± 40 km and an average core mass density of 5200 ± 1000 kg/m^3. The large error bars on these estimates are due to the poorly constrained S-wave velocity profile at the base of the mantle and to mislocation errors of deep moonquakes. The detection of horizontally polarized S waves reflected from the core and the absence of detection of vertically polarized S waves favour a liquid state in the outermost part of the core. All these results are consistent, within their error bars, with previous estimates based on lunar rotation dissipation (Williams et al., 2001) and on lunar induced magnetic moment (Hood et al., 1999).

© 2011 Elsevier B.V. All rights reserved.

1. Introduction

The radius of Earth's core has been relatively precisely determined more than one century ago from the analysis of seismic data (Oldham, 1914), only 17 years after the first measurement on a seismogram (von Rebeur-Paschwitz, 1889). But more than 40 years of negative attempts and processing efforts have been necessary before the publication of the first reported observations of seismic core phases in the Apollo seismic data (Weber et al., 2011). However, the results of this pioneering paper in which some inconsistency between the discontinuity radii deduced from different body waves remains, must be confirmed by a more precise analysis which integrates the trade-off between the mantle seismic velocities and the core size, and the constraints on the body wave ampli-

tudes. Note also that Love numbers were only computed a posteriori and not integrated in the model inversion. As the radius of the core is a key parameter for constraining scenarios of Moon formation by a giant impact (Benz et al., 1989; Canup and Asphaug, 2001), its precise determination will greatly improve our understanding of the geometry and dynamics of such giant and catastrophic impact, providing crucial constraints on the state of primordial Earth's mantle. Prior to Weber et al. (2011), none of the published seismic models (Toksoz et al., 1974; Nakamura et al., 1976, 1982; Khan and Mosegaard, 2002; Khan et al., 2007; Lognonné et al., 2003; Gagnepain-Beyneix et al., 2006) have put direct constraints on the lunar core radius, and only indirect constraints were achieved. Those come from the observations of magnetic signals related to the lunar's core magnetic field rejection (Russell et al., 1982; Hood et al., 1999) and from the inversion of geodetic data (Hood and Jones, 1987; Mueller et al., 1988; Kuskov and Kronrod, 1998; Kuskov et al., 2002), including the Love numbers (Williams et al., 2001; Khan et al., 2004; Khan and Mosegaard,

* Corresponding author at: Université de Toulouse, UPS-OMP, IRAP, Toulouse, France. Tel.: +33 5 61 33 30 45; fax: +33 5 61 33 29 00.
  E-mail address: garcia@dtp.obs-mip.fr (R.F. Garcia).

2005). Among these constraints, the difference between the spin of the polar axis and the Cassini spin state measured by Williams et al. (2001) is central for suggesting a liquid core. So far, the suggested values of this lunar liquid core radius range from 250 km to 450 km.

Constraints on the core composition are even much weaker, as the end member values for its size lead to either pure iron core for the smallest values, to ilmenite core for the largest ones (see for example Lognonné and Johnson (2007) for the trade-off of core models verifying both the mantle seismic constraints and the global geodetic ones). The seismically inverted temperature at the bottom of the mantle provided by Gagnepain-Beyneix et al. (2006), Khan et al. (2007) are all lower than the pure iron liquidus temperature, suggesting that some light elements must be present in the core if it is liquid. These two models however neither include the Love numbers nor core seismic phases, even though these two types of information could directly constrain the size of the core in their inversions.

In this study, we investigate the seismic structure of the lunar interior following a two-step approach. First, we construct a set of acceptable seismic models of the Moon constrained by mass, moment of inertia, Love numbers and arrival times of P and S waves measured by the Apollo passive seismic experiment. Then, we estimate the core radius by detecting core reflected S wave arrivals from waveform stacking methods. The final result is a preliminary reference model for the Moon, that includes the size and average density of the core.

2. Construction of seismic Moon models

This section describes the construction and selection of the best radial seismic lunar models. These models are described by a small number of parameters, respecting a set of a priori geophysical equations and fitting seismological and geodesic observations. The aim is to obtain the best physical models for each core radius and use them to detect core reflected phases.

2.1. A priori information

The radial models are constructed in order to fit exactly the lunar mass $M_o = 7.3458 \times 10^{22}$ kg (Konopliv et al., 2001; Goossens and Matsumoto, 2008). The crustal model is extracted from Gagnepain-Beyneix et al. (2006) seismic model (see Fig. 1). Crustal density (ρ_c) below the 1 km thick regolith layer is assumed to be constant and
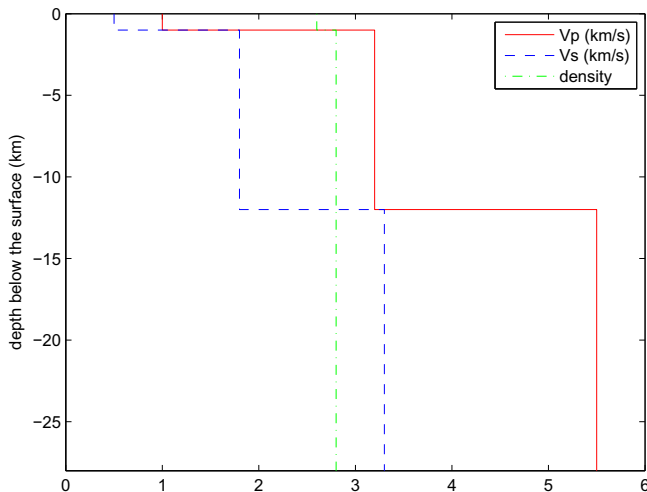

Fig. 1. A priori crust model extracted from Gagnepain-Beyneix et al. (2006) assuming a constant density inside the crust below the 1 km thick regolith layer.

allowed to vary in order to fit geodesic observations. The strong degree one crustal thickness variation is taken into account by assuming a Moho depth of 28 km below the Apollo network (on the near side) in order to fit seismic observations, and an average Moho depth of 40 km (Chenet et al., 2006) in order to fit geodesic observations. Studies of lunar gravity and topography constrain both the average crustal thickness and the density contrast between the crust and the mantle. However, these parameters are correlated. Assuming an average Moho depth of 40 km, the density contrast between crust and mantle is predicted to be about 0.55 (Chenet et al., 2006; Wieczorek et al., 2006). This value is taken as an a priori for the construction of the radial Moon models.

The lunar mantle is assumed to be homogeneous and without any phase transition. This assumption is strong, but if the composition of the lunar mantle is close to Earth's mantle, no phase change of major silicate constituents is expected in the pressure and temperature ranges of the Moon mantle. In addition, previous investigations of lunar mantle chemistry based on seismic data did not detect any strong chemical composition variation with depth (Khan et al., 2007), suggesting that the 550 km depth discontinuity, reported in earlier models (Nakamura, 1983; Khan and Mosegaard, 2002), is weakly resolved by the Apollo data set (Lognonné and Johnson, 2007). In addition, we assume an adiabatic temperature gradient in the lunar mantle. Even if not fully valid in the middle and upper mantle, where the temperature profile is mainly conductive (Gagnepain-Beyneix et al., 2006), the adiabatic hypothesis is expected to generate no more than a few percent of differences in seismic velocities (Bina, 2003) which is smaller than the typical error of lunar seismic models. Assuming homogeneity and adiabaticity of the lunar mantle, we can use the Adams–Williamson equation to derive the density profile of the Moon mantle:

$$\frac{d\rho}{dr} = -\frac{\rho(r)g(r)}{\Phi(r)} \tag{1}$$

where r is the radius, $\rho(r)$ the volumic mass, $g(r)$ gravity, and $\Phi(r)$ the seismic parameter given by:

$$\Phi(r) = V_P^2(r) - \frac{4}{3}V_S^2(r) \tag{2}$$

where $V_P(r)$ and $V_S(r)$ are respectively the P and S wave velocities. If we assume a state of hydrostatic equilibrium for the lunar interior, pressure variations are described by:

$$\frac{dP}{dr} = -\rho(r)g(r) \tag{3}$$

where $P(r)$ is pressure. Consequently, if seismic velocities are known, the above equations can be integrated from top to bottom in order to construct gravity, pressure, and density profiles, using the additional relation between gravity and density:

$$g(r) = \left(\frac{r_o}{r}\right)^2 g_o - \frac{4\pi G}{r_o^2}\left(\frac{r_o}{r}\right)^2 \int_r^{r_o} \rho(u)u^2 du \tag{4}$$

where G is the gravitational constant, r_o the average Moon radius (1737.1 km) and $g_o = \frac{GM_o}{r_o^2}$ the surface gravity. This procedure has been used since the early sixties in order to produce density models of Earth's interior assuming a starting value of density ρ_o (Alterman et al., 1959). In order to link seismic wave velocities to density, a Birch law (Birch, 1964) is used:

$$V_P(r) = a + b\rho(r) \tag{5}$$

where a and b are assumed to be constant because the mantle is assumed to be homogeneous. In addition, because the P-wave to S-wave velocity ratio increases with depth in previous Moon seismic models (Nakamura et al., 1982; Khan and Mosegaard, 2002; Log-

nonné et al., 2003; Gagnepain-Beyneix et al., 2006), it is assumed to vary linearly with radius according to:

$$\frac{V_P(r)}{V_S(r)} = A + Br \tag{6}$$

For given values of density at the top of the mantle ($=\rho_c + 0.55$), Birch law parameters (a and b), and P–S velocity ratio parameters (A and B), a seismic model of the mantle predicting $V_P(r)$, $V_S(r)$ and $\rho(r)$ can be constructed down to the core.

For a given value of core radius (R_{core}), and using the lunar Mass, the average core density (ρ_{core}) is deduced.

The procedure described above allows us to build seismic and density profiles of the lunar interior obeying simple physical laws with only 6 parameters: crust density (ρ_c), Birch law parameters (a and b), P–S velocity ratio parameters (A and B) inside the mantle, and core radius (R_{core}). These parameters are gathered in a model vector $\mathbf{m}$. Average core density is computed in order to fit exactly the mass of the Moon. Only models with core density in the range [4.0–10.0] kg/cm^3, and fitting both Love numbers $k_2 = 0.0213 \pm 0.0025$ and $h_2 = 0.039 \pm 0.008$ (Williams, 2007; Goossens and Matsumoto, 2008) and polar moment of inertia ratio $IR = 0.3932 \pm 0.0002$ (Konopliv et al., 2001) within their error bars will be selected.

In order to construct physical Moon models, the 6 parameters are explored following ranges and steps given in Table 1. The range of crustal density (ρ_c) is defined according to previous estimates (Gagnepain-Beyneix et al., 2006; Chenet et al., 2006). Birch law parameters are explored between values corresponding to the Earth upper mantle as defined in PREM ($a = -7.4146$ and $b = 4.5872$) (Dziewonski and Anderson, 1981) and IASP91 ($a = -10.7346$ and $b = 5.5743$) (Kennett and Engdahl, 1991) reference Earth models. P wave to S wave velocity ratio is explored around the value obtained for a Poisson solid ($\sqrt{3} \approx 1.73$). The ranges for origin (A) and slope (B) of its variation with radius are chosen in order to allow either decrease or increase with depth, and variations around values obtained in previous models. Core radius is explored from 250 km to 490 km.

2.2. Best radial Moon models

The next step is to select the best radial Moon models that fit both P and S arrival times and geodesic observations. In order to let the core radius as a free parameter, a best radial Moon model will be obtained for each core radius.

Then, for each core radius, an exploration of the five remaining parameters is performed with a neighbourhood algorithm (NA) (Sambridge, 1999) with ten randomly selected starting models and performing twelve iterations of NA with parameters ns = 30 and nr = 3. These parameters mean that at each iteration the neighbourhoods of the three best models are explored with 10 new random models. The cost function to minimize is defined as the sum of χ^2 functions of seismic travel times and geodesic observations (Love numbers and polar moment of inertia ratio):

Table 1
Summary of parameter ranges explored in the construction of physical Moon models.

Parameter	Range	Step
Crust density (kg/cm^3) (ρ_c)	[2.6 3.0]	–
Birch law origin (a)	[−10.74 −7.41]	–
Birch law slope (b)	[4.58 5.57]	–
$\frac{V_P}{V_S}$ law origin (A)	[1.0 2.95]	–
$\frac{V_P}{V_S}$ law slope (km^{-1}) (B)	[−0.000662 0.0004]	–
Core radius (km) (R_{core})	[250 490]	5

$$J(\mathbf{m}) = \frac{1}{Ns} \sum_{i}^{Ns} \frac{\left(t_i^{obs} - t_i^{calc}\right)^2}{\sigma_i^2}$$
$$+ \frac{1}{3} \left(\frac{\left(h_2^{obs} - h_2^{calc}\right)^2}{\sigma_{h_2}^2} + \frac{\left(k_2^{obs} - k_2^{calc}\right)^2}{\sigma_{k_2}^2} + \frac{\left(IR^{obs} - IR^{calc}\right)^2}{\sigma_{IR}^2} \right) \tag{7}$$
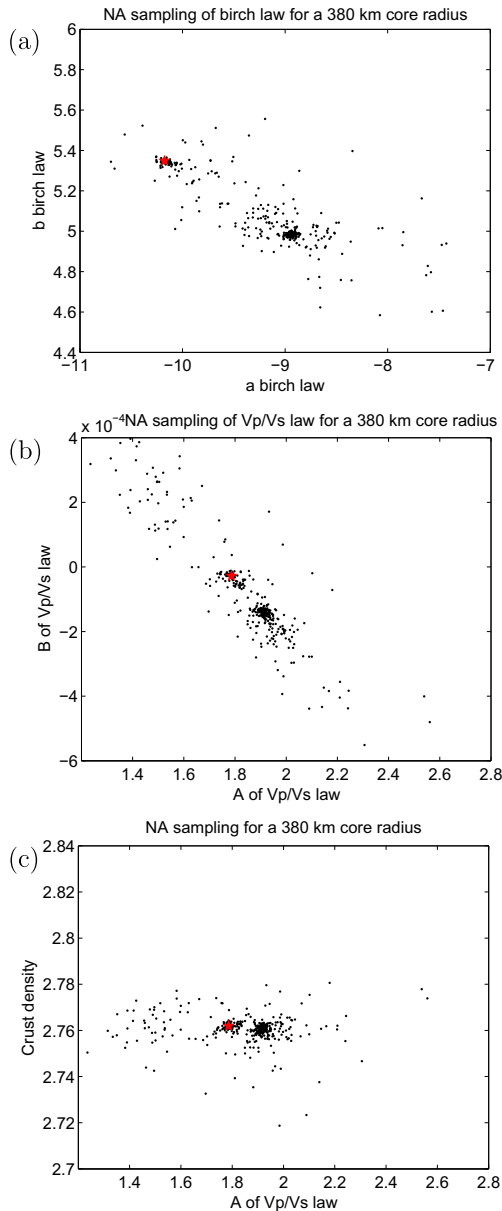
with t_i^{obs} the observed travel time of the seismic phase (including both P and S phases), t_i^{calc} the predicted travel time inside model $\mathbf{m}$, σ_i^2 the travel time error, Ns the number of travel time measurements; and h_2^{obs}, h_2^{calc}, k_2^{obs}, k_2^{calc}, IR^{obs}, IR^{calc}, σ_{h_2}, σ_{k_2} and σ_{IR}, respectively observed and calculated values of h_2 and k_2 Love numbers, polar moment of inertia ratio and corresponding errors. The first part of the right hand side of Eq. (7) will be referred to as χ_{seismo}^2, whereas the second part as χ_{geod}^2. This cost function gives an equal weight to seismological and geodetic observations in order to construct a reference model constraining both density and seismic velocities.

The h_2^{calc}, k_2^{calc} and IR^{calc} values are computed during model construction. However, in order to be fully consistent, the computation of χ_{seismo}^2 requires relocation of all natural seismic events, and correction for P and S wave shallow structure below the seismic stations. Therefore, for each physical model tested, the P and S wave traveltimes given by Lognonné et al. (2003) are inverted in order to relocate the events and to obtain P and S wave station corrections of zero average. Only arrival time data with errors smaller than 10 s are kept. A total of 343 P and S travel times from 64 events (8 artificial impacts, 19 meteor impacts, 10 shallow events and 27 deep moonquakes) are used. The inversion is performed with a damped Gauss–Newton algorithm (Tarantola, 1987) with starting event location parameters given by Gagnepain-Beyneix et al. (2006) and zero station corrections. The χ_{seismo}^2 value of P and S wave travel times obtained after inversion is computed for each physical model tested.

Results of the inversion are summarized in Figs. 2–4. Fig. 2 gives an example of the parameter space sampling by NA algorithm for a core radius of 380 km. The sampling by NA algorithm explores the volume of parameter space. Fig. 3a plots the minimum values of the cost function $J(\mathbf{m})$, χ_{geod}^2 and χ_{seismo}^2 obtained for each core radius. The best models for core radius between 300 km and 400 km give a similar fit of the seismological and geodesic observations. For core radius smaller than 300 km, the fit of seismological observations is slightly degraded. For core radius larger than 400 km, χ_{geod}^2 at minimum value of the cost function increases with radius, reflecting the difficulty to fit geodesic observations with large core radii. Fig. 3b plots the variation with radius of the P and S wave velocities and density for the best models obtained for each core radius. A comparison with the starting model of Gagnepain-Beyneix et al. (2006) shows that the fit of geodesic observations favours S wave velocities at the bottom of the mantle higher than previously inferred. Fig. 4 presents the correlation between parameters obtained for the best radial models. Birch law parameters are strongly correlated between themselves, but not with core radius. $\frac{V_P}{V_S}$ ratio presents an increase with depth consistent with previous investigations. The parameters describing the variations of $\frac{V_P}{V_S}$ ratio are correlated between themselves, but there is no significant correlation with core radius. The crust density is almost constant around 2.76 kg/cm^3. It means that, despite large variations of Birch law parameters, imposing the average crustal thickness (40 km) and the density jump at the crust/mantle interface (0.55 kg/cm^3) strongly constrains the average crust density in a radial model consistent with geodesic observations. However, an average crust density of 2.76 kg/cm^3 is consistent with our assumptions and with previous estimates (Chenet et al., 2006).

Fig. 2. Example of parameter space sampling by NA algorithm for a core radius of 380 km; (a) sampling projected into the plane of a and b Birch law parameters, (b) sampling projected into the plane of A and B parameters of $\frac{V_p}{V_s}$ ratio law, (c) sampling projected into the plan of α and ρ_c parameters. Each dot represents a model vector and best model values are indicated by a red star. (For interpretation of the references in colour in this figure legend, the reader is referred to the web version of this article.)

The core density is correlated with core radius with high densities for small core sizes and low densities for large core sizes. Overall, geodesic and travel time data poorly constrain the size of the core, which motivated us to look for additional constraints that could come from core reflected phases.

3. Modelling core reflected phases

This section demonstrates that the core radius can be constrained by the detection of horizontaly polarized S waves reflected on the core (ScSH) and precise the data set that be can be used for such a detection. The data and signal processing methods allowing ScSH wave detections are described in the next section.

3.1. Waveform modelling

We focus on SH waves reflected on the core because, if the upper part of the lunar core is fluid (Williams et al., 2001), their energy is completely reflected back to the surface. Ray theoretical amplitudes of body waves are computed including geometrical spreading and attenuation (see last table of the paper for values of quality factor). As shown in Fig. 5a, ScSH amplitude at the recording station is of the order of 10–20% of the direct SH wave amplitude depending on the attenuation model and assuming similar amplitudes radiated at the source. Deep moonquakes with best signal to noise ratio (mainly A01, A06 and A07 events) are assumed to be driven by tides (Cheng and Toksoz, 1978; Araki, 2001). A recent analysis of the focal mechanism of these events, which is based on a model that fits only occurence times of the events, suggests fault plane orientations with a dip angle between 60° and 70° with large error bars (Weber et al., 2009). However, studies of these events based only on observations of P and S wave amplitudes and polarities favour focal mechanisms with a horizontal focal plane (Nakamura, 1978; Koyama and Nakamura, 1980). As shown in Fig. 5b, these focal mechanisms have a maximum of SH energy radiated along the vertical direction, which correspond to the take-off angles of ScSH wave.

In contrast, direct SH waves have a smaller excitation at the source. Consequently, for such source mechanisms, the ScSH/SH amplitude ratio is close to one in the 50–80° epicentral distance range. Moreover, those mechanisms generate SH wave and ScSH wave of opposite polarities at the source. Due to the change in polarity resulting from reflection at the core surface, these two body waves should thus have the same waveform. This waveform similarity can also be used as a posterior constraint to validate the ScSH wave detection.

In contrast, vertically polarized S waves will lose part of their energy when reflected at the core surface due to conversion into P waves reflected and transmitted at this interface. Smaller amplitudes for ScSV waves than for ScSH waves are thus expected, as observed on Earth.

3.2. Error propagation

The deep moonquake records present a low signal to noise ratio. Records allowing P and S arrival detections are obtained only after stacking many individual records from the same deep moonquake cluster. Owing to this low signal to noise ratio, to the low number of stations, and to the uncertainty on the radial seismic model, the error bar on the event location coordinates are usually quite large (see Table 2). In order to minimize the effect of mislocation errors and seismic structure just below the stations, ScS-S differential times are used. These differential times present a low sensitivity to the structure below the station because S and ScS waves have similar crustal delays. In addition, these differential times also present a low sensitivity to event mislocations along latitude and longitude coordinates, even if, as we will see below, this sensitivity is non-zero. Because the largest error is on the quake depth, and because this parameter is strongly influencing the ScS-S differential time (hereafter called t_d), the event depth will be determined simultaneously with the core radius. However, ScS-S differential times alone do not allow us to relocate the lateral position of the event. Therefore, the stacking process can be effective only if the errors on latitude and longitude of the events generate relative ScS-S differential time variations between stations smaller than half the dominant period of the records, in order to ensure coherent (in phase) stack of the body waves. The differential time ScS-S at one station for an event location different from the theoretical one may be written:
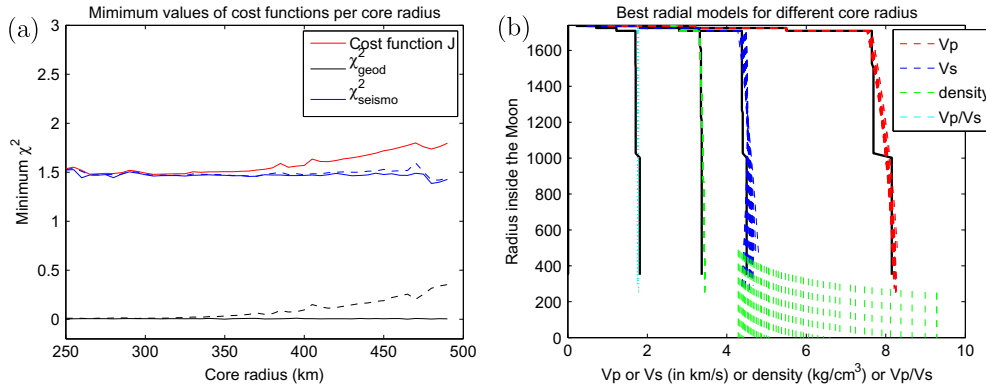
Fig. 3. (a) Minimum values of cost function $J(\mathbf{m})$ (in red), χ^2_{geod} (in black) and χ^2_{seismo} (in blue) obtained for each core radius. Values of χ^2_{geod} (black dashed line) and χ^2_{seismo} (blue dashed line) corresponding to minimum values of the cost function $J(\mathbf{m})$ are also plotted. (b) P-wave (in red) and S-wave (in blue) velocities (in km/s), density (in green) and $\frac{V_p}{V_s}$ ratio (light blue) of the best models obtained for each core radius (dashed lines). The model of Gagnepain-Beyneix et al. (2006) is plotted as plain black lines for comparison. (For interpretation of the references in colour in this figure legend, the reader is referred to the web version of this article.)

$$t^j_d(\theta_0 + \delta\theta, \phi_0 + \delta\phi) = t^j_d(\theta_0, \phi_0) + \Delta t_d + \delta t^j_d \qquad (8)$$

where (θ_0, ϕ_0) are the (latitude,longitude) theoretical coordinates of the event, $\Delta t_d = \frac{1}{N}\sum_j^N \left(t^j_d(\theta_0 + \delta\theta, \phi_0 + \delta\phi) - t^j_d(\theta_0, \phi_0) \right)$ is the average differential time shift residual over all the stations due to the event mislocation, and $\delta t^j_d = t^j_d(\theta_0 + \delta\theta, \phi_0 + \delta\phi) - t^j_d(\theta_0, \phi_0) - \Delta t_d$ is the differential time shift residual of station j relative to this average. The second term on the right hand side produces a shift of all the ScS-S differential times that is displacing the ScS stack relative to its theoretical position, whereas the last term on the right hand side produces relative shift between the stations that may generate incoherent stacks if it is larger than half the dominant period of the body wave. The relative ScS-S differential time variations between stations i and j is defined by $R\delta t^{ij}_d = \delta t^i_d - \delta t^j_d$. Table 2 presents an estimate of the maximum values $\left(\text{Max}\left(R\delta t^{ij}_d \right) \right)$ and standard deviations $\left(\text{Std}\left(R\delta t^{ij}_d \right) \right)$ of relative ScS-S differential time variations between stations inside the one standard deviation error ellipse of event positions. These values are controlled by the error on the event location, but also by the event position relative to the stations. When the back azimuth of the event is approximately the same for all the stations (event outside the network area), Δt_d may be large, but $R\delta t^{ij}_d$ values remain small. In contrast, for an event located in the middle of the network, Δt_d is small, but $R\delta t^{ij}_d$ values present large variations.

Owing to the instrument response of Apollo stations, the largest dominant period ensuring a good signal to noise ratio is about 2.5 s. Therefore, the only events for which the stacking process is expected to work properly according to the error on lateral event coordinates are events A01, A06, A07 and A44. In addition, detection by stacking process is more reliable if 4 stations are available. Consequently, only deep moonquake stacks for events A01, A06 and A07 can possibly allow ScSH reliable detections.

4. Data and methods

This section describes the data and method used to detect SH waves reflected from the lunar core surface. First, the stacking process of individual deep moonquake records along X and Y horizontal sensors is described. Then, a new method, based on the energy equipartition inside the coda waves, is applied to correct for relative gain variation between X and Y horizontal sensors. In addition the site response below the station is corrected, and data are filtered in the frequency range with highest signal to noise ratio. Finally, the stacking process is described, and bootstrap validations of the results are presented.

4.1. Stacks of deep moonquake individual records

Individual records of deep moonquakes are first aligned by cross-correlation of the vertical component and the horizontal component with the best S/N ratio. The part of the individual records presenting spikes have been removed by hand from the stacks. As a result, the number of individual records stacked varies with time along the stack. However this method is probably the best one to ensure that no biases are introduced by a spike correction method. The number of individual records stacked depends on the seismic station and on the deep moonquake nest. This number is usually comprised between 20 and 100. An example of deep moonquake stack is presented in Fig. 6 which shows the stacks of deep moonquake cluster A01 on the vertical component of Apollo 12 station.

4.2. Correction of the gain of horizontal sensors

The horizontal components of ground velocity are recorded by two different sensors (X and Y) of Apollo LP seismometers. Because these sensors may have slightly different gains, the rotation of X and Y components in order to reconstruct radial and transverse components may be biased. In order to correct for this effect, X/Y amplitude ratios were computed for each station in the coda of seismic events with high signal to noise ratios. Because of the high level of seismic scattering in the lunar crust, the seismic wavefield in the coda of lunar quakes is approximately in equipartion state (Larose et al., 2005; Sens-Schönfelder and Larose, 2008). Thus, if the gains of the two sensors were identical, and assuming only radial variations of seismic scattering properties, we should observe the same energy level on the two horizontal components (Margerin et al., 2009), and the X/Y ratio in the coda should be equal to one. If not, the X/Y ratio gives an estimate of the gain ratio of the two sensors. A limitation to this analysis is a small correlation between the horizontal components of the Apollo 12 seismometer discovered by Vinnik et al. (2001). However, this study also indicates that this correlation is not observed on the other Apollo stations. Fig. 7 gives an estimate of the X/Y ratio for the different stations measured in the coda of different seismic events. The coda signal is defined here by the part of the records starting at least 100 s after the S wave arrival. The X/Y ratio is estimated by different methods (see legend of Fig. 7), and it presents only small variations as a function of time inside the coda. For stations S12 and S14, the codas of artificial impacts created by Lunar modules and stage IV of Saturn V rocket were used because of high signal to noise ratio for these events. For stations S15 and S16, deep moonquake codas with high signal to noise ratios were added to artificial impacts. The X/Y ratio of
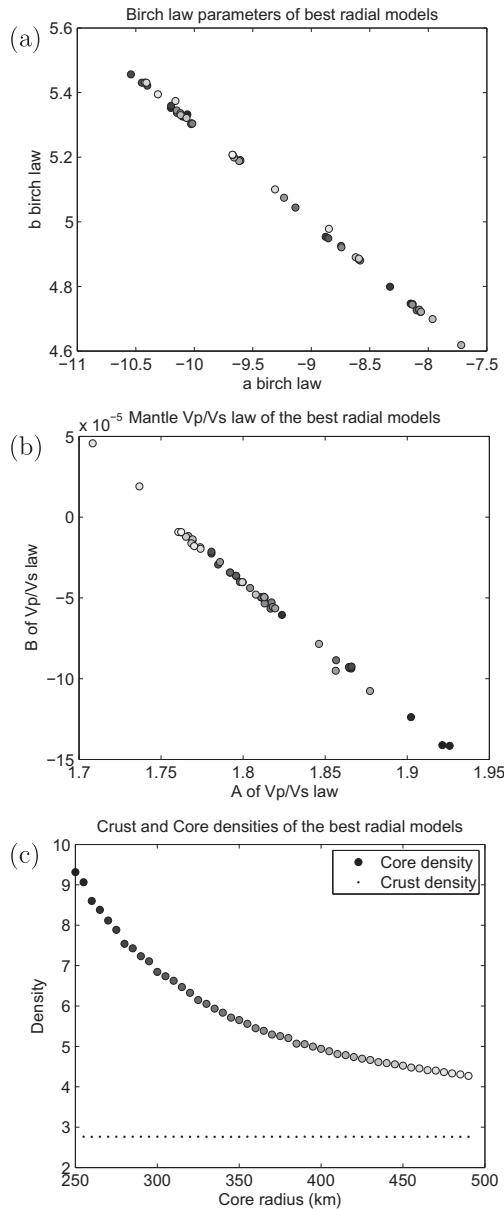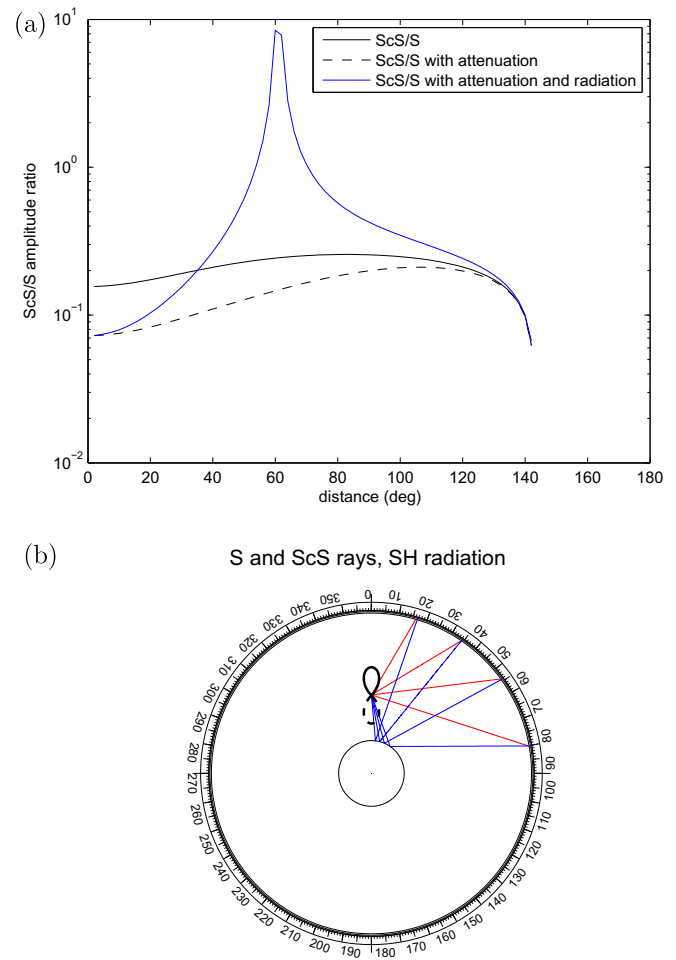
Fig. 4. Correlations between parameters when considering the best radial models; (a) best values of *a* and *b* Birch law parameters, (b) best values of *A* and *B* parameters of $\frac{V_p}{V_s}$ ratio law, (c) crust and core densities as a function of core radius (in km) for the best radial models. Colour scale of circles goes from black to white with increasing core radius parameter.

Fig. 5. (a) ScS/S amplitude ratio without (plain line) and with (dashed line) attenuation, assuming same radiation pattern at the source; and with attenuation and radiation from an horizontal fault plane (blue line). Computations are performed in the seimic model of Gagnepain-Beyneix et al. (2006) with an S wave quality factor of 300 below 770 km depth and (b) examples of S (in red) and ScS (in blue) ray paths for a 900 km depth event. The radiation pattern (in black) of SH waves for a displacement perpendicular to the figure along an horizontal fault plane is surperimposed, with plain line for positive values, and dashed line for negative values. (For interpretation of the references in colour in this figure legend, the reader is referred to the web version of this article.)

different events is almost constant for artificial impacts (before 1973), but it presents strong variations for deep moonquakes (after 1973) possibly due to both a lower signal to noise ratio and a less diffuse wavefield. However, the relative gain of *X* and *Y* components can be reasonably well estimated for all the stations. For stations S12 and S14, only artificial impacts are taken into account. The *Y* component is then corrected for this instrumental effect before performing the rotation in radial and transverse components for each deep moonquake event.

4.3. Correction of relative frequency responses of the stations

The horizontal component records of seismometers from the Apollo 14 and Apollo 16 missions present frequency contents significantly different from those of Apollo 12 and Apollo 15 missions. Fig. 8a presents a logarithmic average of the power spectral densi-

ties of all the deep moonquake signals selected per seismic station. Apollo 14 seismic station presents an additional spectral peak at a frequency of 0.87 Hz, and Apollo 16 seismic station presents lower energy at low frequency compared to Apollo 12 and 15 stations. These anomalous features observed on the two horizontal sensors are not present on the vertical components of the records (not shown). It suggests that this effect is mainly due to the response of the ground just below the stations (site response). However, in order to be able to use the phase of the records in stacks, these records must have a similar frequency content. The spectral amplitudes of S14 and S16 transverse components have thus been corrected by a spectral amplitude ratio computed between these stations and an average value between stations S12 and S15. The power spectral densities obtained after correction are presented in Fig. 8b. These corrections of S14 and S16 records give a power spectral density similar to stations S12 and S15.

4.4. Data filtering

S waves usually have more energy at lower frequencies. Moreover, we expect both the crustal scattering and the attenuation to

Table 2
Summary of data used in this study. Parameters are the following: latitude, longitude and depth of the quake, and corresponding errors (Gagnepain-Beyneix et al., 2006), initial number of stations available, number of stations selected after removing bad quality records, parameters $Max(R\delta t_d^{ij})$ and $Std(R\delta t_d^{ij})$.

| Event name	Lat. (deg)	Long. (deg)	Depth (km)	Δlat. (deg)	Δlon. (deg)	Δdepth (km)	Init. # stat.	# Stat. sel.	$Max(R\delta t_d^{ij})$ (s)	$Std(R\delta t_d^{ij})$ (s)
A01	−17.44	−38.37	917	1.1	0.6	11	4	4	1.82	1.1
A05	−31.04	−44.92	902	3	3	80	2	2	1.34	–
A06	49.7	54.69	860	1	0.7	11	4	4	1.57	0.9
A07	23.97	53.7	900	0.8	0.7	12	4	4	1	0.94
A08	−27.97	−28.08	940	2	1.2	21	1	1	–	–
A09	−37.8	−30.85	975	4	2.6	43	3	2	8.56	–
A10	34.01	−28.04	1139	3	3	80	2	2	0.57	–
A11	9.6	19.49	1233	0.8	0.7	12	3	2	0.73	–
A14	−28.7	−33.94	880	1.7	1.3	22	3	2	4.34	–
A15	−0.94	−2.96	885	3	3	80	3	3	13.39	8.8
A16	6.79	5.14	1105	1.2	0.7	18	3	3	2.26	1.55
A17	23.08	−17.97	861	2.6	0.4	15	3	3	7.51	5.27
A18	18.56	34.72	882	1.8	0.9	24	3	2	3.4	–
A19	15.96	37.91	841	3	3	80	3	2	9.46	–
A20	21.72	−41.01	1055	2.4	0.8	13	3	3	4.32	2.83
A21	−15.8	−43.49	1060	3	3	80	2	1	–	–
A24	−36.85	−38.9	980	2.1	1.7	32	4	3	4.91	2.49
A25	34.4	59.3	898	2	1.7	26	4	4	2.57	2.1
A26	12.19	10.22	1135	1.5	0.7	20	3	2	1.5	–
A27	22.51	18.53	1059	1.9	1.4	14	4	2	3.49	–
A28	32.69	11.64	720	3	3	80	3	1	–	–
A30	11.78	−34.26	921	1.5	1	23	4	4	1.87	2.03
A33	6.89	117.75	887	1.5	1.3	30	3	2	0.46	–
A34	7.04	−9.28	932	1.2	0.6	26	3	3	3.8	2.58
A41	13.9	−26.79	953	5.6	2.2	84	3	1	–	0
A42	22.68	−53.46	1004	1.8	1.4	24	3	2	3.94	–
A44	51.85	57.08	956	5.8	1.9	20	3	3	1.98	0.78

be reduced at low frequencies. Consequently, the Apollo data recorded in peaked mode were converted into the long period mode by using theoretical responses of these two acquisition modes, and filtered by an order 3 butterworth band pass filter with corner frequencies at 0.3 Hz and 0.9 Hz. This operation allows us to enlarge and equalize the available frequency band. The frequency limits have been chosen by trial and error in order to minimize the high frequency signal, and to reduce as much as possible the lower cut off frequency. Below 0.3 Hz and above 0.9 Hz, the noise dominates the signal in stacks of Apollo deep moonquake data.
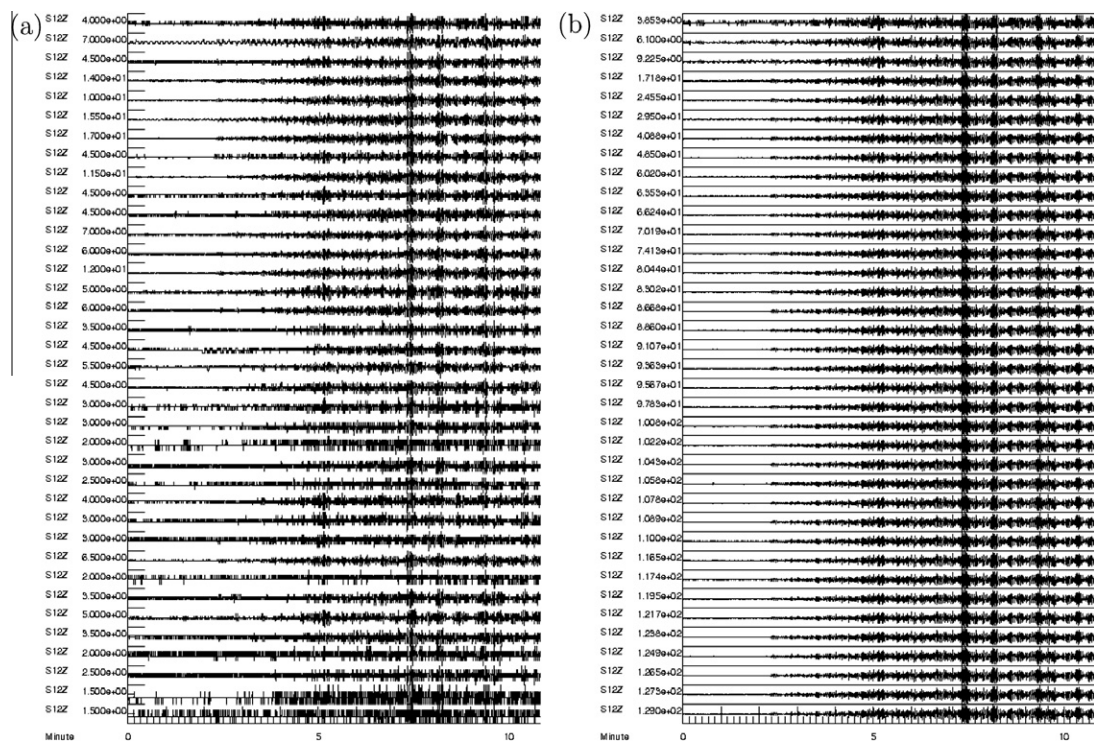
Fig. 6. (a) Examples of individual records of events belonging to deep moonquake cluster A01 and recorded on the vertical component of station Apollo 12 after alignment by cross-correlation. (b) Evolution of the stack as a function of the number of records stacked. From top to bottom each line includes a new record in the stack. The numbers on the left of each trace give the maximum amplitude of the trace expressed in Apollo digital units.
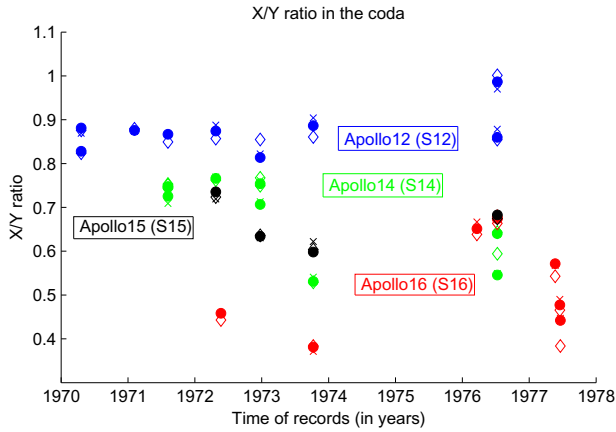
Fig. 7. X/Y amplitude ratios in the coda of different seismic events as a function of event origin time (in years). Event origin times after 1973 correspond to deep moonquakes. X/Y ratios are computed with different methods: time average of X/Y logarithm (filled circles), median of X/Y logarithm (crosses) and signal energy ratio (open diamonds). The average X/Y ratios are 0.856 ± 0.012, 0.748 ± 0.010, 0.661 ± 0.035, 0.533 ± 0.044, respectively for seismic stations S12 (in blue), S14 (in green), S15 (in black) and S16 (in red). (For interpretation of the references in colour in this figure legend, the reader is referred to the web version of this article.)

Fig. 9 presents power spectral densities of the signals before and after the filtering process.

4.5. About polarisation filtering

Weber et al. (2011) used polarisation filtering in order to detect body wave arrivals reflected by deep Moon discontinuities. We evaluate the performance of this filter for picking S waves and detecting reflections from deep Moon discontinuities.

The polarisation filtering described in Weber et al. (2011) is a non-linear method allowing to enhance linearly polarized seismic arrivals. Assuming $\frac{V_S}{V_P}$ ratio equal to 0.5 in the lunar regolith (Gagnepain-Beyneix et al., 2006), P and S body waves are linearly polarized for incidence angles smaller than $60° = \sin^{-1}\left(\frac{V_S}{V_P}\right)$ (Nuttli, 1961). Therefore, this method can be applied to most teleseismic P and SV wave arrivals on the Moon. However, assuming that SH waves are present only on the transverse component, such filtering is useless for these waves.

The radial (R) and transverse (T) components are computed from X and Y records by the following relation, assuming that X

and Y sensors are aligned, respectively along East and North directions (the real orientations of the sensors is given in Table 3):

$$\begin{bmatrix} R \\ T \end{bmatrix} = \begin{bmatrix} \sin\theta & \cos\theta \\ -\cos\theta & \sin\theta \end{bmatrix} \times \begin{bmatrix} X \\ Y \end{bmatrix} \tag{9}$$

where θ is the azimuth of the event at the receiver. In the following we will note the real (true) displacements with superscripts T and the measured displacements without superscript, and assume that $Y = Y^T$ and $X = \gamma X^T$. The gain corrections for the horizontal components has been presented above, and γ is equal to the X/Y ratio determined previously. If this correction is not applied before the rotation of X and Y components, the relations between measured radial and transverse components and the true ones is the following:

$$\begin{bmatrix} R \\ T \end{bmatrix} = \begin{bmatrix} \gamma\sin\theta & \cos\theta \\ -\gamma\cos\theta & \sin\theta \end{bmatrix} \times \begin{bmatrix} \sin\theta & -\cos\theta \\ \cos\theta & \sin\theta \end{bmatrix} \times \begin{bmatrix} R^T \\ T^T \end{bmatrix} \tag{10}$$

In particular, the radial component can be expressed as $R = a_{11}(\gamma)R^T + a_{12}(\gamma)T^T$ with $a_{ij}(\gamma)$ being the terms of the matrix A corresponding to the matrix product described above.

The polarisation filter (Weber et al., 2011) can be written as $OZ_j = Z_jM_j$ and $OR_j = Z_jM_j$, respectively along the vertical and radial components, with $M_j = \sum_{i=-n}^{n} Z_{j+i}R_{j+i}$, where j is the time step and $n = 6$. Now assuming that SV body wave has a motion W_j^S and an incidence angle j_o, and that ϵ_z and ϵ_r are respectively the noise on the vertical and radial component, the true vertical and radial components can be written as $Z_j^T = W_j^S \sin(j_o) + \epsilon_z$ and $R_j^T = W_j^S \cos(j_o) + \epsilon_r$. Reporting these equations in (10), and assuming $Z = Z^T$, we obtain

$$Z_jR_j = \left(W_j^S\sin(j_o) + \epsilon_z\right)\left[a_{11}(\gamma)W_j^S\cos(j_o) + a_{11}(\gamma)\epsilon_r + a_{12}(\gamma)T^T\right] \tag{11}$$

Consequently, the non-linear polarisation filter is subject to two different noise sources. First, the term $a_{12}(\gamma)T^T$ perturbs the radial component. Second, the SV wave signal should be over the noise level along the vertical component ($W_j^S\sin(j_o) \gg \epsilon_z$) in order to ensure enhancement of the SV wave signal. Our tests demonstrate that the first noise source due to wrong rotation in the horizontal plane is generally negligible because γ is close to one. Fig. 10 presents the polarisation filtering performed on raw deep moonquake stacks after rotation for event A01 and station S15. This figure can be compared directly to figure S1 of Weber et al. (2011). SV wave signal is clearly enhanced by the polarisation filtering both on OZ and OR because the SV wave signal is clearly dominating noise on both vertical and radial components. Such a clear enhancement
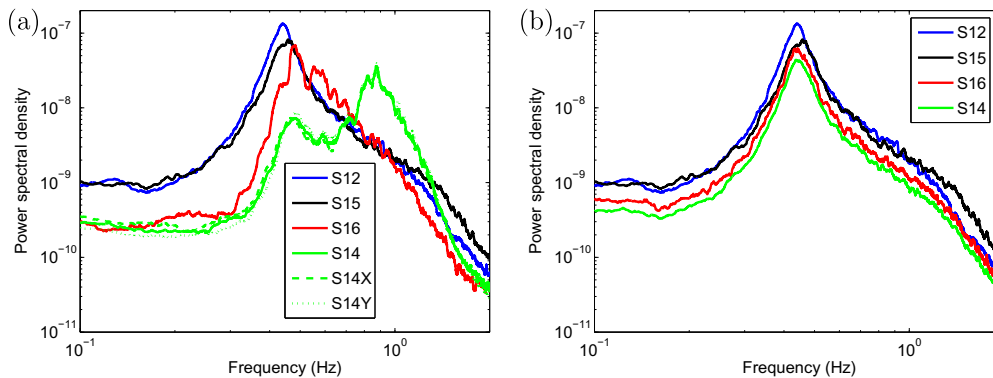
Fig. 8. Logarithmic average of power spectral densities over all deep moonquake transverse records before (a) and after (b) correction of S14 and S16 transfer functions as a function of frequency for seismic stations S12 (in blue), S14 (in green), S15 (in black) and S16 (in red). On the left, curves for sensors X (dashed green) and Y (dotted green) of station S14 are also presented. All the curves have been smoothed by a moving average filter over 251 points in order to clarify the figures. Amplitude differences are due to differences of energy between the different deep moonquake records. (For interpretation of the references in colour in this figure legend, the reader is referred to the web version of this article.)
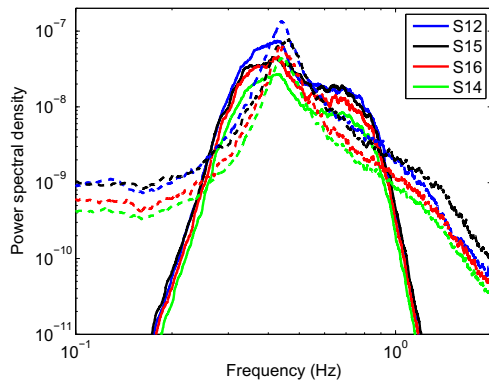
Fig. 9. Logarithmic average of power spectral densities over all deep moonquake transverse records before (dotted lines) and after (plain lines) modes conversion and filtering as a function of frequency for seismic stations S12 (in blue), S14 (in green), S15 (in black) and S16 (in red). All the curves have been smoothed by a moving average filter over 251 points in order to clarify the figures. (For interpretation of the references in colour in this figure legend, the reader is referred to the web version of this article.)

of SV pulse by polarisation filtering is not observed in Weber et al. (2011) study. This comparison suggests that the stacks of individual deep moonquake signals coming from the same deep moonquake cluster (A01 in this case) was performed differently between the two studies.

Because the polarisation filtering is able to enhance the coherent SV wave signal on both radial and vertical components, we can use this information in order to refine the arrival time picks of SV waves and to infer the length of the SV pulse. Fig. 11 presents

Table 3
Azimuth (in degree) of X and Y sensors extracted from Apollo Scientific Experiments Data Handbook available at http://nssdc.gsfc.nasa.gov/planetary/online_books.html.

Station name	X azimuth (in deg.)	Y azimuth (in deg.)
S12	180	270
S14	0	90
S15	0	90
S16	334.5	64.5

a focus on the polarisation filtering of radial components around the SV arrival. The SV wave arrivals are clearly enhanced by this process on both the raw and filtered records. More interestingly, the SV pulse length can be estimated in the 5–10 s range, and it looks to be varying more with event number than with station number. This observation suggests that the pulse length reflects more the properties of the signal coming from the source region than the variation of scattering properties below the stations.

However, P and S waves reflected back from discontinuities at radius smaller than 500 km inside the Moon have incidence angles smaller than 2°. Therefore, the amplitude of the SV wave on the vertical component is predicted to be at best 4% of the one on the radial component. Due to the high coda energy and to the low signal to noise ratio of deep moonquake stacks, the SV wave signal coming from deep reflectors inside the Moon will be smaller than the noise on the vertical component $\left(W_j^S \sin(j_o) \ll \epsilon_z\right)$. The same argument also holds for deep reflections arriving as P waves at the station. In this case, the polarisation filtering will only enhance time intervals for which the noise (or coda signal) is in phase on both components.
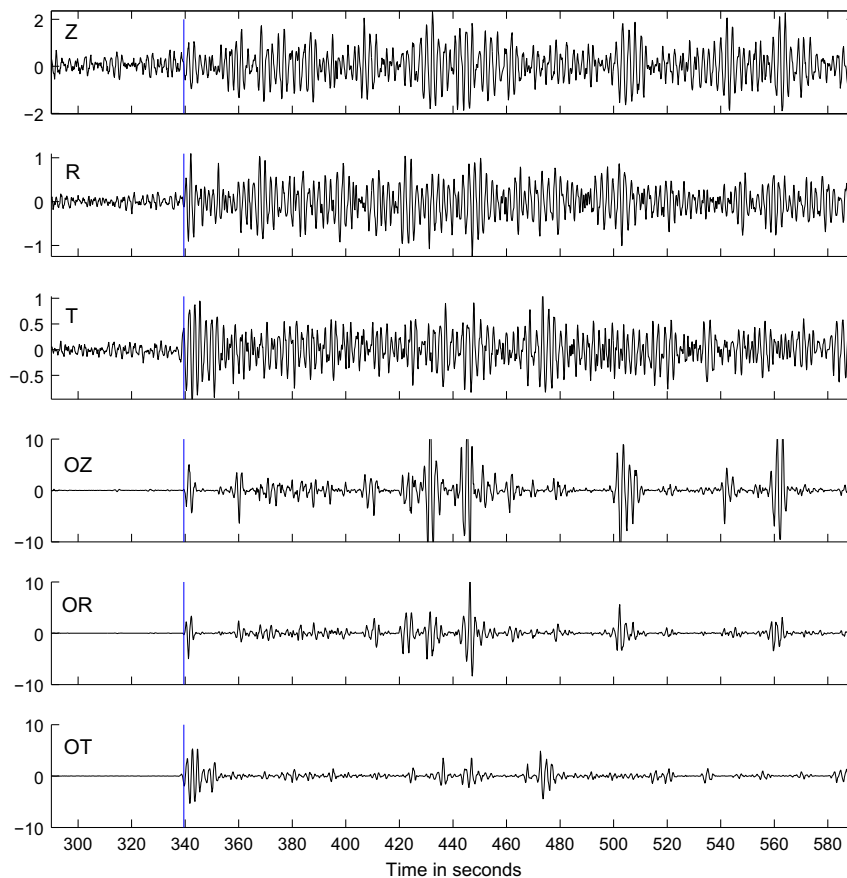
Fig. 10. (Top three traces): Raw deep moonquake stacks components (cluster A1) at Apollo station 15. (bottom three traces): Polarisation filtered components of the same stack. S wave arrival time predicted by our best model (blue line) is presented. (For interpretation of the references in colour in this figure legend, the reader is referred to the web version of this article.)
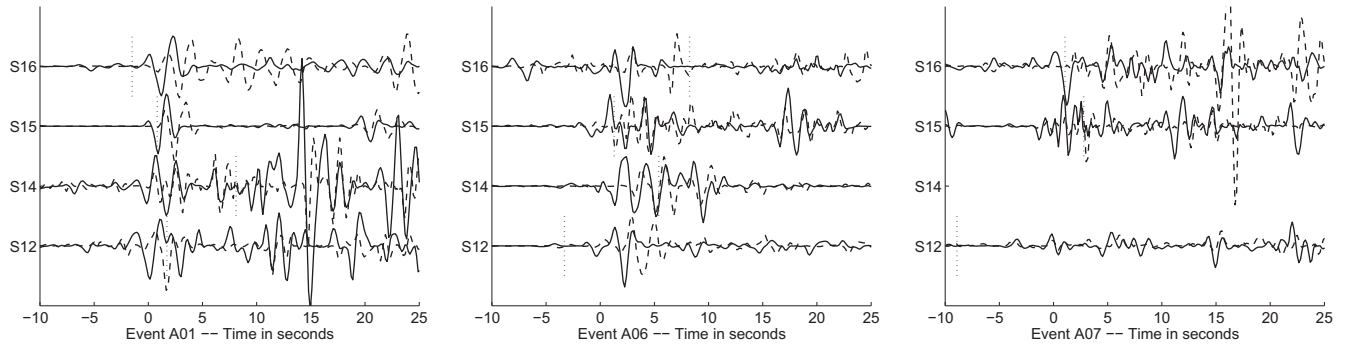
Fig. 11. Polarisation filtering of radial components (OR_j) aligned on the hand picked SV wave arrival times for raw records (dashed lines) and records after filtering (plain lines). From top to bottom, records of stations S12, S14, S15 and S16. From left to right, records for events A01, A06 and A07. The vertical component of station S14 for event A07 is not available in our data base, consequently the polarisation filtering cannot be performed. The vertical dotted lines indicate the S wave arrival time predicted by our best Moon model.

In conclusion, the polarisation filtering is useless for ScSH wave detection. It gives good results for SV and P waves when the incidence angle is not too small, and allows us to estimate the length of the S pulse in the 5–10 s range. However, it cannot be used for the detection of waves reflected by deep discontinuities inside the Moon because in this case the noise dominates the signal on one component, and both OZ and OR filtered signals present enhancements for time intervals for which Z and R codas are in phase. For all these reasons, we decided not to use this method for ScSH wave detection.

4.6. S wave alignment and differential travel time computations

The arrival times of S waves on the transverse components of deep moonquake stacks are hand picked by visual inspection of vertical, radial and transverse components. During this process, the polarity of some records has been changed in order to ensure similar polarities of S waveforms for the different records of the same deep moonquake. The stacks of deep moonquake records strongly depend on the S wave arrival time. In order to obtain a very precise alignment of SH wave between the different stations, the records are inverted by a non-linear method searching for optimal SH waveform and relative delay times between the stations (Chevrot, 2002). Results of this waveform matching procedure are presented in Fig. 12. Interestingly, the best matching waveform presents significant energy on a length that is consistent with the SV pulse lengths obtained by polarisation filtering ($\approx$5 s for A01, $\approx$7 s for A06, $\approx$10 s for A07). The SH hand picks are corrected by delays deduced from this analysis.

The arrival times of S and ScS waves are computed inside the best radial models for each core radius using the deep moonquake relocations obtained for these models. These computations are performed by a new implementation of the Tau-P algorithm (Buland and Chapman, 1983; Calvet and Chevrot, 2005).

4.7. Stacking process

All the waveforms are aligned on the S wave arrivals and normalized to maximum amplitude of the first one hundred seconds of the coda. Again, events with less than four recording stations and events for which horizontal location errors produce relative differential times between stations larger than half the dominant period ($\approx$1.25 s) are excluded. Only high quality events A01, A06 and A07 are kept. The stacks of the waveforms for each event are performed by computing the differential times ScS-S for a given moonquake depth D_i and a given core radius R_{core} using the corresponding best radial model. After alignment and stack, the ScSH waveform energy is computed in a 10 s window after the predicted arrival time on the stacked trace. This process is repeated for all the best radial models obtained previously corresponding to core radii between 250 km and 490 km with a 5 km step, and for event depth in the ±400 km range around the epicenter location with a 2 km step. Such a process allows us to compute, for each event i, $NRJ_i^{ScS}(R_{core}, D_i)$ the energy of stacked ScS waveforms depending on core radius R_{core} and event depth D_i. The semblance of the stacked records is also defined as the ratio between the stacked ScS waveform energy and the average energy of the records used to perform the stack (Neidell and Taner, 1971). This parameter is
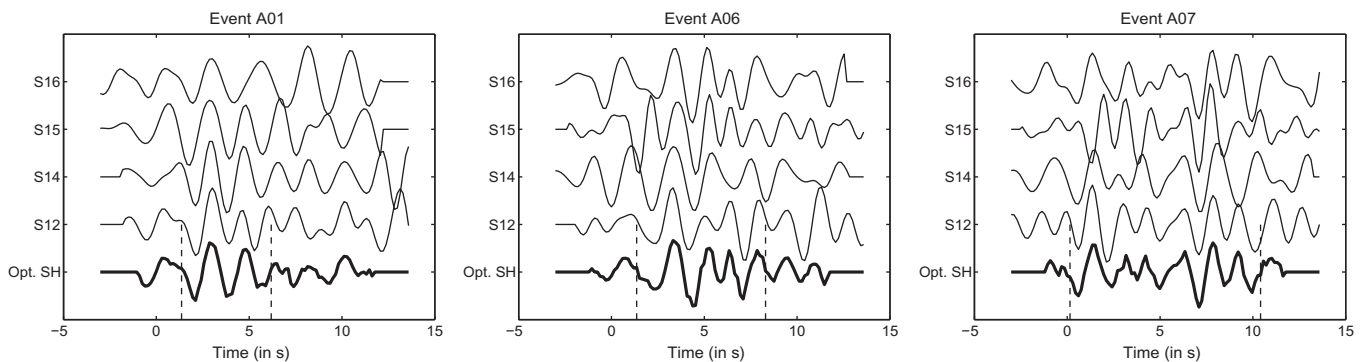
Fig. 12. Results of the SH wave optimal waveform and delay times inversion. From bottom to top, optimal SH waveform (thick line) and filtered records of stations S12, S14, S15 and S16 after optimal alignment. From left to right, records for events A01, A06 and A07. Vertical dashed lines delimit the time interval with maximum coherent energy which is used below to define the optimal SH waveform.

varying between zero (complete destructive interference) and one (fully constructive interference), providing a measure of stack efficiency normalized to the energy of the records. As for the energy, the semblance depends on core radius R_{core} and event depth D_i: $SEMB_i^{ScS}(R_{core}, D_i)$.

In order to include additional a priori information on the events depth, stacked energies and semblances are multiplied by a gaussian function of the form $G_i(D_i) = \exp\left(-\frac{(D_i - D_i^0)^2}{\sigma_i^2}\right)$ with D_i^0 the a priori event depth and ΔD_i^0 its error. The standard deviation of the gaussian is defined by $\sigma_i = 10\Delta D_i^0$, in order to allow large variations around the a priori event depth. A priori deep moonquake locations and related errors on the parameters are extracted from the study by Gagnepain-Beyneix et al. (2006). This weight function $G_i(D_i)$ is only a smooth way to impose event depth in the $\pm 5\Delta D_i^0$ range around theoretical value.

Fig. 13 shows the ScSH stack energies obtained for the three events A01, A06 and A07. On these plots, a correlation between core radius and event depth is clearly seen. However, the ScSH energy presents a peak in the 380–400 km core radius range for the three events.

Once these energies are computed, their maximum value for each core radius are defined by $NRJmax_i^{ScS}(R_{core}) = \max_{D_i}\left[NRJ_i^{ScS}(R_{core}, D_i)\right]$. These functions are plotted in Fig. 14(a)–(c) for the three events selected. They present a global or local maximum in the 380–400 km core radius range. However, the statistical test performed below demonstrate that, when taken separately, the maxima of these events are statistically significant only for events A06 and A07. To investigate the statistical significance of the results, we consider the average of maximum ScS stack energies of individual events:

$$NRJsum(R_{core}) = \frac{1}{N_{ev}} \sum_{i}^{N_{ev}} NRJmax_i^{ScS}(R_{core}) \qquad (12)$$

with N_{ev} the number of events. However, even if the records are scaled before the stacking process, $NRJmax_i^{ScS}(R_{core})$ functions present different amplitudes for the different events. In our case, $NRJsum(R_{core})$ is dominated by events A01 and A06. In order to give an equal weight to all the events, these functions are scaled to their standard deviation and their mean is substracted before summation in order to produce energy plots including all the events with a similar contribution. The final result is a scaled energy depending only on core radius which is defined for ScS waveform stacks by:

$$\overline{NRJ}sum(R_{core}) = \frac{1}{N_{ev}} \sum_{i=1}^{N_{ev}}$$
$$\times \frac{(NRJmax_i^{ScS}(R_{core}) - \langle NRJmax_i^{ScS}(R_{core})\rangle)}{std(NRJmax_i^{ScS}(R_{core}))} \qquad (13)$$

with < > and $std(\ )$, respectively the average and standard deviation operators. The same operations are performed for the semblance by computing for each event the maximum semblance at different core radius ($SEMBmax_i^{ScS}(R_{core})$) and the average of these curves over all the events ($SEMBsum(R_{core})$). The scaled version of semblance curve does not have to be computed because the semblance measure is already normalized to the energy of the records. Functions $NRJsum(R_{core})$, $\overline{NRJ}sum(R_{core})$ and $SEMBsum(R_{core})$ are presented in panels (d), (e) and (f) of Fig. 14. This figure demonstrates that when the three events are taken together the energy maximas at 380 and 395 km core radius are statistically significant (at three standard deviations level).

In order to test the dependence of the results on the filtering process, the whole process (including S wave alignment) is repeated on the data before acquisition mode conversion and band-
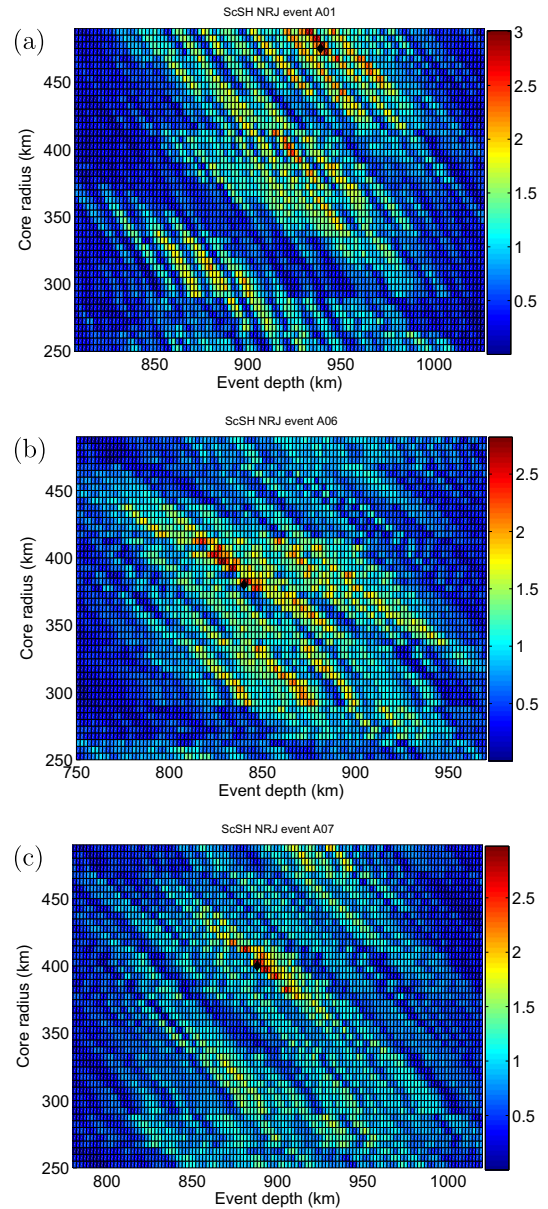
Fig. 13. Stacked energies $NRJ_i^{ScS}(R_{core}, D_i)$ in colour, as a function of core radius (in km) and event depth (in km), for events A01 (a), A06 (b) and A07 (c). The energies are multiplied by a Gaussian function $G_i(D_i)$ centered around a priori depth D_i^0. Colour goes from blue (low energy) to red (high energy), and the maximum value is indicated by a black diamond. (For interpretation of the references in colour in this figure legend, the reader is referred to the web version of this article.)

pass filtering. The results are presented in panels (g), (h) and (i) of Fig. 14. The peaks of ScSH wave energy around 380 and 395 km core radius are also present but less statistically significant. The consistency of the results between the two different frequency ranges strongly argue in favour of a ScSH detection. Moreover, the lower ScSH energy at high frequencies (in peaked mode) than at low frequencies (in long period bandpass mode) justifies the search for this body wave at frequencies as low as possible.

Because the ScSH wave stacks may be slightly shifted inside the ten seconds time window, the core radius obtained may be also shifted. For example, if the energy of ScSH wave stack inside the window is significant only 2 or 3 s after the beginning of the window, S-ScS travel time is under-estimated and core radius over-estimated. In order to remove this effect, the records obtained after filtering have been deconvoled from the optimal source time
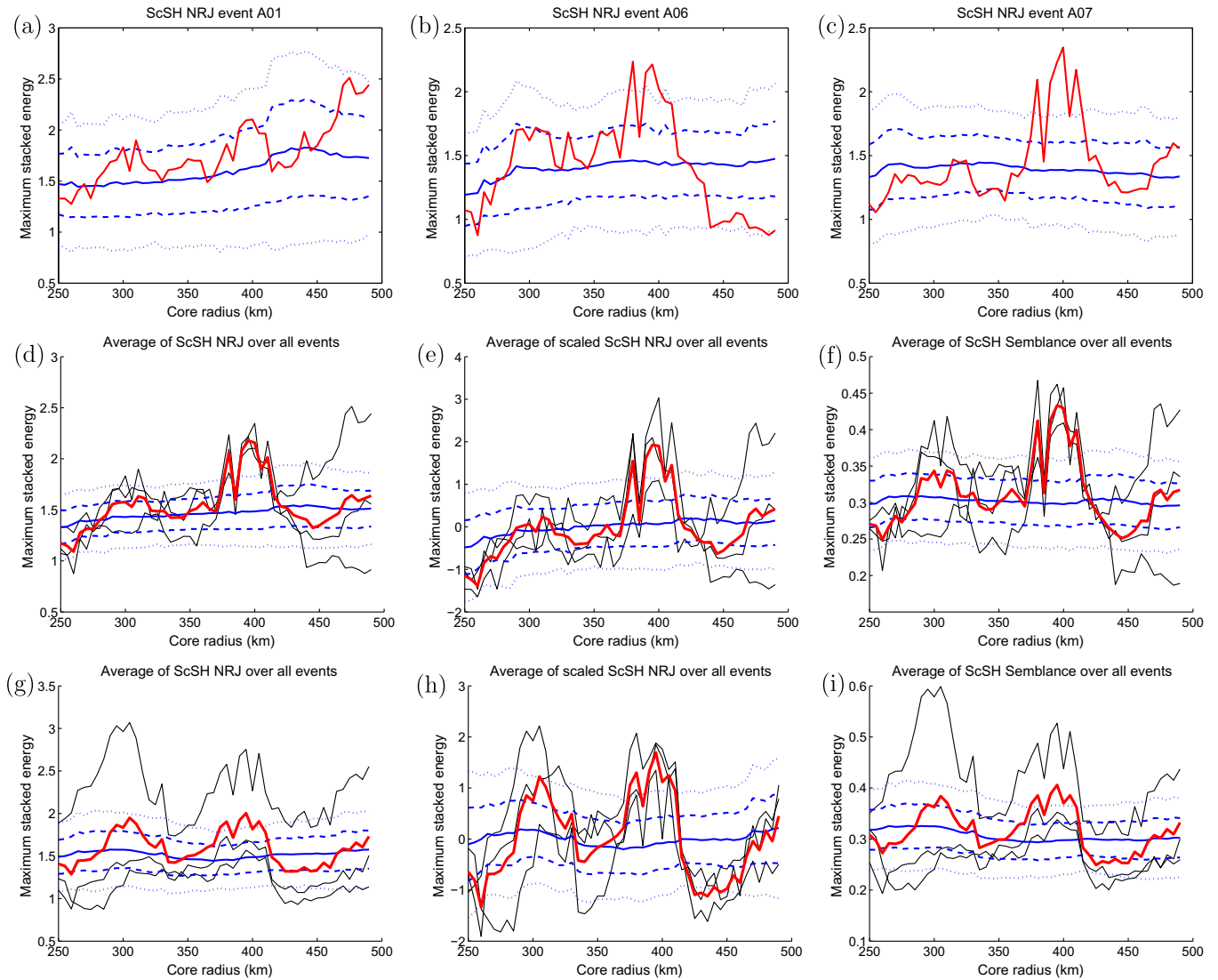
Fig. 14. Plots of stacked maximum energies NRJmax$_i$(R_{core}) for events A01 (a), A06 (b), A07 (c), and the average of these energies NRJsum(R_{core}) (d), the scaled average of these energies $\overline{\text{NRJ}}$sum(R_{core}) (e) (red curves), and the average semblance SEMBsum(R_{core}) (f) (red curve). Panels (g), (h) and (i) are identical, respectively to panels (d), (e) and (f), but for data before acquisition mode conversion and bandpass filtering. The average value (blue plain line), the one standard deviation around this value (blue dashed lines) and the two standard deviation value (blue dot-dashed line) obtained for the bootstrap ensemble are shown on each plot. On panels (d), (e), (f), (g), (h) and (i) curves for individual events (thin black lines) are also presented. (For interpretation of the references in colour in this figure legend, the reader is referred to the web version of this article.)

functions presented on Fig. 12. After deconvolution, SH energy is focused on a 2 s window. The stacking process is reproduced by computing energy on a 2 s window centered on the ScS arrival. The results are presented in Fig. 15, for the three different moon-quakes. Clear maximas of ScSH energy are obtained for events A06 and A07, but at slightly smaller core radius (370–390 km), which suggests that the over-estimation of the core radius due to the 10 s window may be real. However, the small size of stacking window has the drawback to focus the stack energy in a very narrow core radius range. Due to quake mislocations and also possibly to lateral heterogeneities at the base of the lunar mantle, the real ScS-S differential travel times vary from one event to the other and different core radius are obtained for the different events. As a consequence, the three curves do not interfere constructively when summed together.

The test presented above and the increasing difficulty to explain geodesic observations with increasing core radius above 380 km, favour a core radius value at the lowest range of the broad energy peak observed on Fig. 14. Optimal core radius estimate is 380 km,

with a 30 km error bar estimated from the range of core radius for which the energy is above the two standard deviation level.

A similar exercise is also done for the radial components of the records in order to detect ScSV waves. The results obtained on filtered data are presented on Fig. 16. As expected, ScSV wave is not detected inside the S coda because its amplitude is smaller than ScSH one. This exercise also demonstrates that the bootstrap method described below is pertinent for the validation of ScSH detections.

4.8. Validation of the results with bootstrap

We applied a bootstrap method to test the statistical significance of our results (Efron and Tibshirani, 1993). The SH arrival picks are perturbed randomly in a ±30 s range. We repeat the stacking process for each new data set. We then compute the mean, maximum and standard deviation over 150 random realizations of the resulting stacks of energy. This method gives an estimate of the background noise corresponding to random
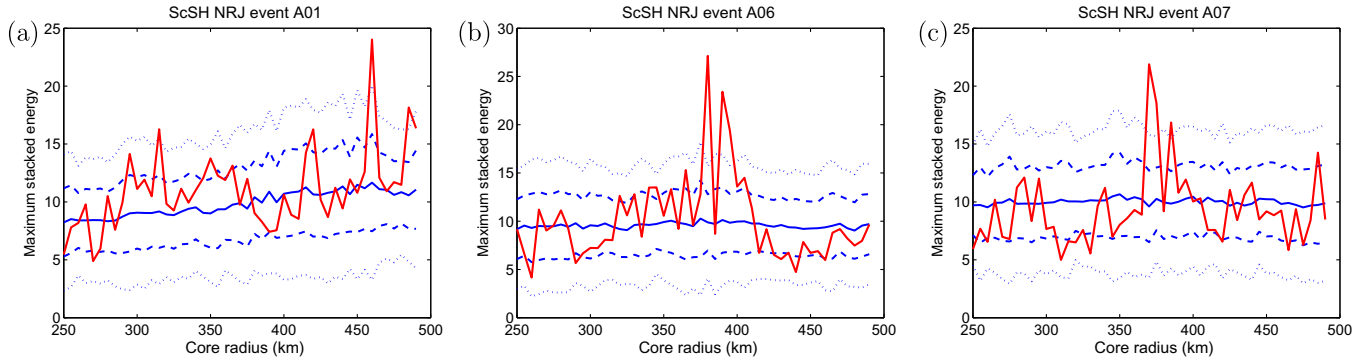
Fig. 15. Plots of stacked maximum energies NRJmax$_i$(R_{core}) after deconvolution of optimal SH waveforms for events A01 (a), A06 (b), A07 (c). The average value (blue plain line), the one standard deviation around this value (blue dashed lines) and the two standard deviation value (blue dot-dashed line) obtained for the bootstrap ensemble are shown on each plot. (For interpretation of the references in colour in this figure legend, the reader is referred to the web version of this article.)
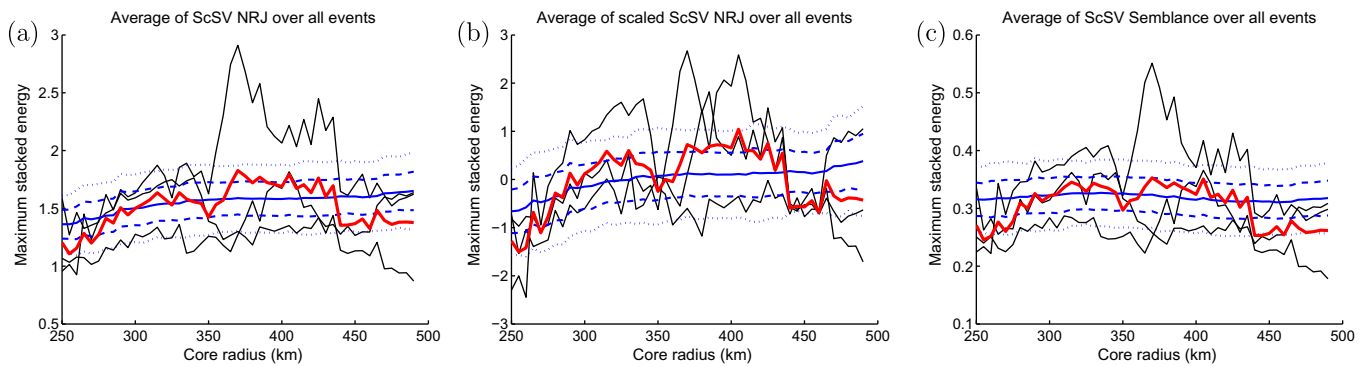
Fig. 16. Plots of NRJsum(R_{core}) (a), $\overline{NRJ}$sum(R_{core}) (b) and SEMBsum(R_{core}) (c) (red curves) for stacks of the radial components of the records. The average value (blue plain line), the one standard deviation around this value (blue dashed lines) and the two standard deviation value (blue dot-dashed line) obtained for the bootstrap ensemble are shown. Curves obtained for individual events (thin black lines) are also presented. (For interpretation of the references in colour in this figure legend, the reader is referred to the web version of this article.)

waveform alignment. A peak can be considered significant if it is above two standard deviations of the bootstrap ensemble.

As described previously, the two standard deviation level is passed in the 380–400 km core radius range for filtered data using a 10 s window (Fig. 14), and in the 370–390 km core radius range after deconvolution of optimal SH waveforms for events A06 and A07. The statistical validation is obtained for ScSH detection and not for ScSV detection. Moreover, an error estimate of ±30 km is provided. This error will be evaluated more precisely below.

4.9. Stacked waveforms comparison

Fig. 17 presents record sections of transverse components aligned on predicted ScSH arrival for a 380 km core radius. After alignment on ScSH, the waveforms are stacked in order to produce a ScSH stacked waveform for each event. Similar processing is also done for the SH wave. The comparison of these stacked waveforms is shown in Fig. 18. In this figure, the SH and ScSH waveforms have been cross-correlated on a 10 s window, and are presented for the best correlation within a ±2 s time shift of ScSH stack. This shift correspond to the value of Δt_d due to the error on the (longitude, latitude) coordinates of the quake, and it should be below 2 s for the events processed in this study. A good correlation between ScSH and SH stacks is obtained for events A06 and A07, but it is low for event A01. This waveform similarity, already enhanced by the success of stacking after deconvolution of SH optimal waveform, gives further support for a ScSH detection.

5. Discussion

5.1. Error estimates

Fig. 14 provides a formal error estimate on the core radius which takes into account the uncertainty in the stacking process, and errors on the depth of the events. However, the error on the seismic model must also be taken into account in order to estimate its effect on the core radius. From the set of models generated by the NA algorithm at 380 km radius, we compute the maximum and minimum values of seismic velocities and densities at each depth inside the ensemble of models within the half width of the probability peak. These values define the error bars on the best radial model. They are plotted on Fig. 19a. These error bars are almost constant inside the mantle for density and P-wave velocity with a relative error of respectively 0.2% and 3.3%. However, the error on S-wave velocity presents a minimum in the mid-mantle (3%) and a maximum (11%) at the base of the mantle. The strong increase in S-wave velocity errors at the base of the mantle translates to a significant error on the absolute value of core radius. Considering a vertically incident ScS wave from a deep moonquake at a depth of 900 km, the integrated error on the S-wave velocity profile below the event produces an error on the ScS travel time of about 9% on the two-way travel time from the event to the core, or about 19 s. This travel time error can be translated directly into an error on the core radius of approximately 33 km. This rough estimate is probably an upper estimate because the vertical incidence of ScS rays has the highest sensitivity to core radius.
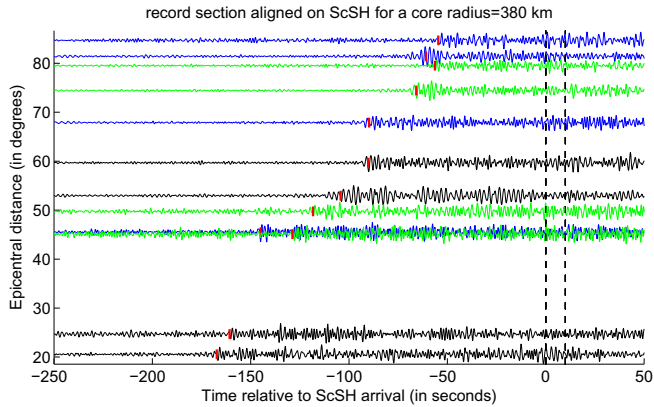
Fig. 17. Record sections of transverse components plotted as a function of epicentral distance (in degrees) and time relative to predicted ScSH arrival time for a 365 km core radius (in seconds). Red marker indicate the SH wave arrival time pick. Vertical dashed lines indicate the 10 s window used to stack ScSH waveforms. Different colours are used for the different quakes: A01 in black, A06 in blue and A07 in green. (For interpretation of the references in colour in this figure legend, the reader is referred to the web version of this article.)

However, it highlights the difficulty to obtain an absolute value of core radius without S-wave arrival time measurements at large epicentral distances. Taking into account the true ray geometries, and the bootstrap analysis of ScSH wave detection, the error bar on the core radius is about 40 km.

The error on the average core density for a 380 km core radius is about 0.3 kg/cm³. By looking at Fig. 4c, varying the core radius in a range of ±40 km around its best estimate gives approximately two times larger average core density variation than the error bar estimate at 380 km core radius. Moreover, because the core density is inferred from mass and moment of inertia, and due to the low value of the core moment of inertia (of the same order as the error bar on the moment of inertia of the whole planet), small variations of crustal thickness and density may generate large variations of core density. The average crustal thickness is not inverted here, but the error on this parameter requires to increase our estimate of the error on the core density. Consequently, a conservative estimate of average core density is 5.2 ± 1.0 kg/cm³.

5.2. Comparison with previous results

Our estimates of core radius at 380 ± 40 km and average core density at 5.2 ± 1.0 kg/cm³ are respectively at the upper and lower
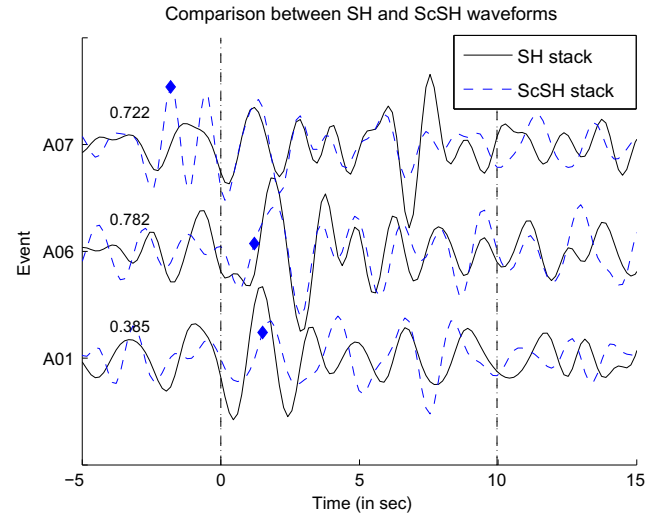
Fig. 18. Comparison between SH (black plain line) and ScSH (blue dashed line) stacks as a function of time and event number. The ScS stacks are aligned for best correlation in the ±2 s range. Blue diamonds indicate the start of ScS stack window before alignment. Events numbers are 1 for A01, 2 for A06 and 3 for A07. Correlation coefficient over the 10 s window is indicated along the stack before the stack window. (For interpretation of the references in colour in this figure legend, the reader is referred to the web version of this article.)

limits of previous estimates from both lunar laser ranging observations (Williams et al., 2001) and induced magnetic moment of the Moon (Hood et al., 1999). This seismic estimate of core radius is significantly larger than the 330 km proposed by Weber et al. (2011), which in some way indicates a large sensitivity to uncertainties in the seismic model at the base of the mantle and to error propagation. However their large error bars of these core radius estimates cover the domain of previously inferred values. Moreover, the detection of ScSH waves and not ScSV waves supports a liquid core beneath the core mantle boundary, as already suggested by the dissipation of lunar rotation (Williams et al., 2001). The average core density is relatively low and suggests either a high level of light elements in a completely fluid core, or a large core temperature. For example, if the average core density is explained by the presence of sulfur alone, more than 10% are required for the nominal value (Sanloup et al., 2000; Balog et al., 2003). But, when the error bar is taken into account the percent of sulfur content can vary from almost zero to large values. However, because an inner core is expected for thermodynamical reasons (Wieczorek
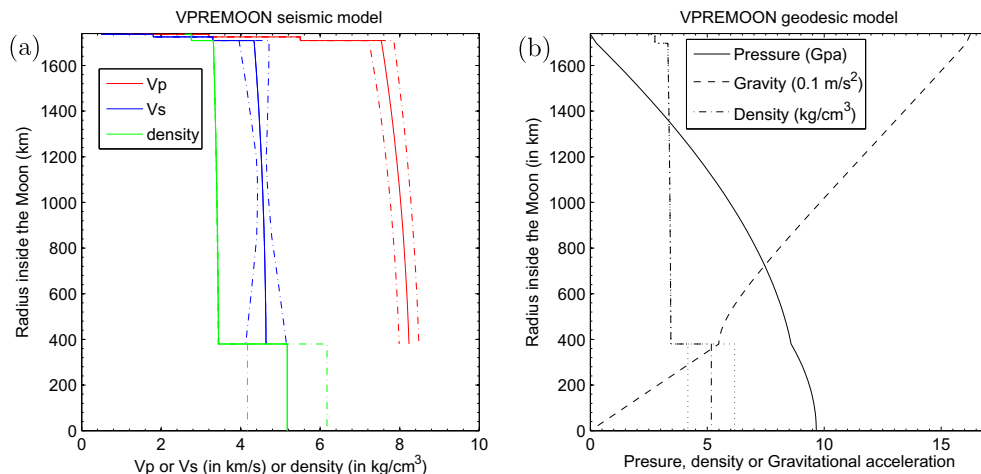
Fig. 19. VPREMOON seismological (a) and geodesic models (b). On the left (a), P and S wave velocities (in km/s) and density (in kg/cm³) are plotted as a function of radius (in km) for the seismological model. The error bars are indicated for each parameters by dot-dashed lines. On the right (b), pressure (in GPa), gravity (in 0.1 m/s²) and density (in kg/cm³) are plotted as a function of radius (in km) for the geodesic model.

Table 4
Location parameters of the event used in the study inside the VPREMOON model.

Event name	Lat. (θ) (in °)	Long. (ϕ) (in °)	Depth (z) (in km)	σ_θ (in °)	σ_ϕ (in °)	σ_z (in km)	Origin date	Origin time (in s)	σ_{t0}(in s)
12LM	−3.94	−21.20	0.0	0.00	0.00	0.0	6911202217	17.70	0.00
13S4	−2.75	−27.86	0.0	0.00	0.00	0.0	7004150209	41.00	0.00
14S4	−8.09	−26.02	0.0	0.00	0.00	0.0	7102040740	55.40	0.00
14LM	−3.42	−19.67	0.0	0.00	0.00	0.0	7102070045	25.70	0.00
15S4	−1.51	−11.81	0.0	0.00	0.00	0.0	7107292058	42.90	0.00
15LM	26.36	0.25	0.0	0.00	0.00	0.0	7108030303	37.00	0.00
16S4	1.30	−23.80	0.0	0.00	0.00	0.0	7204192102	4.00	0.00
17S4	−4.21	−12.31	0.0	0.00	0.00	0.0	7212102032	42.30	0.00
M1	73.52	2.79	0.0	0.64	2.77	0.0	7201040631	19.80	2.48
M2	1.55	−16.91	0.0	0.19	0.19	0.0	7205130846	39.04	0.56
M3	33.02	137.22	0.0	0.93	1.02	0.0	7207172150	56.66	1.29
M4	23.92	10.08	0.0	0.27	0.52	0.0	7207311808	15.23	1.68
M5	15.69	22.44	0.0	1.35	1.21	0.0	7208292258	33.50	2.85
M6	28.85	40.68	0.0	2.51	1.12	0.0	7309262046	16.32	2.88
M7	−24.60	−24.87	0.0	1.00	1.94	0.0	7312241003	19.38	2.93
M8	7.45	−33.32	0.0	0.65	0.90	0.0	7404191830	3.11	2.75
M9	20.23	6.46	0.0	0.41	0.63	0.0	7407171205	2.54	1.57
M10	−7.28	19.78	0.0	0.85	0.72	0.0	7411211315	40.51	2.45
M11	1.68	−8.15	0.0	0.87	0.39	0.0	7412150907	15.15	1.74
M12	−51.80	4.16	0.0	1.22	2.37	0.0	7503052149	22.25	2.92
M13	2.43	43.31	0.0	0.52	0.97	0.0	7504121812	38.22	2.92
M14	−37.16	−121.04	0.0	1.45	1.20	0.0	7505040959	28.51	2.34
M15	−39.24	62.77	0.0	1.79	1.46	0.0	7601130711	22.96	2.63
M16	−16.62	−9.87	0.0	0.96	0.68	0.0	7605280601	56.29	2.44
M17	23.69	−73.88	0.0	1.02	0.99	0.0	7611142313	6.60	2.38
M18	−20.39	−64.47	0.0	0.72	0.94	0.0	7704172332	6.87	2.44
M19	−13.06	−74.91	0.0	5.66	1.23	0.0	7706282222	31.15	2.86
SH1	12.78	50.78	15.9	1.42	2.69	68.6	7209171435	2.96	7.31
SH2	47.79	38.06	8.8	3.14	3.32	37.5	7212062308	33.52	8.23
SH3	−84.71	−137.13	71.3	0.85	1.48	38.6	7303130756	23.63	4.35
SH4	22.35	82.93	0.0	1.66	2.34	7.6	7407110046	19.16	6.53
SH5	26.32	−92.28	0.0	1.58	2.40	6.3	7501030141	56.19	5.10
SH6	65.81	58.96	20.3	1.02	1.13	13.3	7501120313	48.28	4.58
SH7	−16.93	−25.84	127.6	1.62	1.95	85.1	7502132203	50.43	6.68
SH8	44.15	33.94	168.1	2.31	1.84	94.4	7601041118	55.38	6.72
SH9	52.30	−25.83	136.3	0.77	1.08	37.3	7603061012	23.38	2.77
SH10	−18.71	−12.92	79.3	1.13	1.21	80.7	7603081442	10.63	5.28
A01	−17.31	−38.21	918.5	0.58	0.87	8.0	7309300410	58.29	1.40
A06	49.68	54.65	861.2	0.76	0.75	8.1	7607021052	23.70	1.16
A07	23.98	53.64	901.0	0.64	0.62	8.9	7607020311	22.88	1.18
A08	−27.99	−28.03	939.9	1.61	1.34	18.4	7705161052	28.80	3.00
A09	−37.71	−30.71	974.5	2.21	3.30	33.8	7704161958	3.76	4.89
A11	9.29	17.47	1200.4	0.68	0.76	10.3	7706180501	15.12	2.03
A14	−28.65	−33.80	880.6	1.22	1.32	15.8	7305281853	12.49	3.13
A16	6.83	5.07	1104.2	0.63	0.91	13.4	7210081524	35.05	2.04
A17	23.09	−18.00	861.1	1.20	1.32	13.3	7211070852	7.86	2.14
A18	18.56	34.66	882.1	1.39	0.92	18.6	7301052250	29.71	2.17
A20	21.72	−40.88	1055.3	0.63	1.83	10.5	7205151718	6.50	2.58
A24	−36.76	−38.81	980.1	1.79	1.68	26.2	7706121817	37.99	3.62
A25	34.33	59.23	899.3	1.52	1.35	19.4	7706092015	6.64	2.32
A26	12.14	10.13	1135.0	0.88	1.03	16.7	7706201450	48.48	3.08
A27	22.48	18.47	1058.7	1.29	1.53	11.0	7705160001	51.18	1.83
A30	11.81	−34.21	921.4	1.00	1.09	16.5	7205170042	45.35	2.37
A33	6.91	117.72	888.1	1.03	1.15	21.5	7210111935	44.93	2.37
A34	7.04	−9.29	931.4	0.65	0.82	18.3	7206141834	26.91	2.89
A40	−1.60	−10.93	885.4	0.88	0.62	17.5	7306272348	35.15	3.05
A41	13.88	−26.64	951.8	2.43	3.31	48.1	7206081616	24.56	7.43
A42	22.69	−53.38	1004.6	1.37	1.32	17.2	7305030152	34.84	2.44
A44	51.51	56.86	956.8	4.06	2.42	14.6	7405190309	3.63	3.71
A50	9.41	−51.45	835.5	1.23	1.63	21.5	7304300105	25.53	4.69
A51	8.85	15.75	887.1	0.55	0.83	18.4	7402180835	27.18	3.41
A84	−10.03	−31.76	862.2	1.97	2.43	17.3	7607221946	28.41	4.56
A85	27.90	59.16	801.7	1.38	2.87	20.2	7707191037	50.84	8.21
A97	−3.39	18.66	999.9	1.74	2.06	18.9	7705190608	21.00	3.51

Table 5
P and S wave station corrections and associated error bars.

Station name	P cor. (in s)	P cor. error (in s)	S cor. (in s)	S cor. error (in s)
S12	−1.034	0.250	−0.229	0.462
S14	1.162	0.230	−0.584	0.413
S15	−0.298	0.279	−0.950	0.468
S16	0.171	0.758	1.763	1.344

Table 6

VPREMOON model: on the left the seismic model and on the right the geodesic model in which Moho depth as been corrected to 40 km. Attenuation parameters are extracted from previous studies (Nakamura and Koyama, 1982; Nakamura et al., 1982) and arbitrarily fixed in the deep mantle. Seismic velocities and attenuation parameters inside the core are arbitrarily fixed by the authors.

Radius (in km)	V_P (in km/s)	V_S (in km/s)	Density (in kg/cm³)	Q_P	Q_S	Radius (in km)	Density (in kg/cm³)	Gravity (m/s²)	Pressure (in GPa)
1737.1	1.00	0.50	2.600	6750.0	6750.0	1737.1	2.600	1.6248	0.0000
1736.1	1.00	0.50	2.600	6750.0	6750.0	1736.1	2.600	1.6245	0.0056
1736.1	3.20	1.80	2.762	6750.0	6750.0	1736.1	2.762	1.6245	0.0056
1725.1	3.20	1.80	2.762	6750.0	6750.0	1725.1	2.762	1.6196	0.0781
1725.1	5.50	3.30	2.762	6750.0	6750.0	1725.1	2.762	1.6196	0.0781
1709.1	5.50	3.30	2.762	6750.0	6750.0	1709.1	2.762	1.6127	0.1825
1709.1	7.54	4.34	3.312	6750.0	6750.0	1697.1	2.762	1.6076	0.2599
1697.1	7.55	4.34	3.314	6750.0	6750.0	1697.1	3.314	1.6076	0.2599
1671.7	7.57	4.35	3.318	9000.0	4000.0	1671.7	3.318	1.5851	0.5086
1647.1	7.59	4.36	3.322	9000.0	4000.0	1647.1	3.322	1.5632	0.7470
1627.1	7.61	4.37	3.325	9000.0	4000.0	1627.1	3.325	1.5454	0.9389
1607.1	7.63	4.38	3.329	9000.0	4000.0	1607.1	3.329	1.5276	1.1290
1587.1	7.64	4.39	3.332	9000.0	4000.0	1587.1	3.332	1.5098	1.3174
1567.1	7.66	4.40	3.335	9000.0	4000.0	1567.1	3.335	1.4920	1.5040
1547.1	7.68	4.40	3.338	9000.0	4000.0	1547.1	3.338	1.4741	1.6888
1527.1	7.69	4.41	3.341	9000.0	4000.0	1527.1	3.341	1.4562	1.8718
1502.0	7.71	4.42	3.344	9000.0	4000.0	1502.0	3.344	1.4338	2.0988
1487.1	7.72	4.43	3.346	9000.0	4000.0	1487.1	3.346	1.4204	2.2321
1461.7	7.74	4.44	3.350	3375.0	1500.0	1461.7	3.350	1.3976	2.4570
1447.1	7.75	4.44	3.352	3375.0	1500.0	1447.1	3.352	1.3845	2.5848
1427.1	7.77	4.45	3.355	3375.0	1500.0	1427.1	3.355	1.3666	2.7583
1407.1	7.78	4.45	3.357	3375.0	1500.0	1407.1	3.357	1.3486	2.9297
1387.1	7.80	4.46	3.360	3375.0	1500.0	1387.1	3.360	1.3306	3.0992
1367.1	7.81	4.47	3.363	3375.0	1500.0	1367.1	3.363	1.3126	3.2666
1347.1	7.82	4.47	3.365	3375.0	1500.0	1347.1	3.365	1.2946	3.4320
1327.1	7.84	4.48	3.368	3375.0	1500.0	1327.1	3.368	1.2766	3.5954
1307.1	7.85	4.49	3.370	3375.0	1500.0	1307.1	3.370	1.2586	3.7566
1287.1	7.86	4.49	3.373	3375.0	1500.0	1287.1	3.373	1.2405	3.9157
1267.1	7.88	4.50	3.375	3375.0	1500.0	1267.1	3.375	1.2225	4.0728
1252.0	7.88	4.50	3.377	3375.0	1500.0	1252.0	3.377	1.2089	4.1899
1231.7	7.90	4.51	3.379	1125.0	500.0	1231.7	3.379	1.1906	4.3454
1207.1	7.91	4.51	3.382	1125.0	500.0	1207.1	3.382	1.1685	4.5308
1187.1	7.92	4.52	3.384	1125.0	500.0	1187.1	3.384	1.1505	4.6791
1167.1	7.94	4.53	3.386	1125.0	500.0	1167.1	3.386	1.1325	4.8252
1147.1	7.95	4.53	3.388	1125.0	500.0	1147.1	3.388	1.1145	4.9690
1127.1	7.96	4.54	3.391	1125.0	500.0	1127.1	3.391	1.0965	5.1106
1107.1	7.97	4.54	3.393	1125.0	500.0	1107.1	3.393	1.0786	5.2499
1087.1	7.98	4.54	3.395	1125.0	500.0	1087.1	3.395	1.0606	5.3869
1067.1	7.99	4.55	3.397	1125.0	500.0	1067.1	3.397	1.0427	5.5215
1047.1	8.00	4.55	3.398	1125.0	500.0	1047.1	3.398	1.0249	5.6539
1027.1	8.01	4.56	3.400	1125.0	500.0	1027.1	3.400	1.0070	5.7838
1002.0	8.02	4.56	3.403	1125.0	500.0	1002.0	3.403	0.9847	5.9436
987.1	8.03	4.57	3.404	1125.0	500.0	987.1	3.404	0.9715	6.0367
961.7	8.04	4.57	3.406	675.0	300.0	961.7	3.406	0.9490	6.1922
947.1	8.05	4.57	3.408	675.0	300.0	947.1	3.408	0.9361	6.2798
927.1	8.06	4.58	3.409	675.0	300.0	927.1	3.409	0.9185	6.3977
907.1	8.07	4.58	3.411	675.0	300.0	907.1	3.411	0.9010	6.5132
887.1	8.08	4.58	3.413	675.0	300.0	887.1	3.413	0.8835	6.6262
867.1	8.08	4.59	3.414	675.0	300.0	867.1	3.414	0.8662	6.7367
847.1	8.09	4.59	3.416	675.0	300.0	847.1	3.416	0.8489	6.8446
827.1	8.10	4.59	3.417	675.0	300.0	827.1	3.417	0.8318	6.9500
807.1	8.11	4.60	3.419	675.0	300.0	807.1	3.419	0.8147	7.0529
787.1	8.12	4.60	3.420	675.0	300.0	787.1	3.420	0.7978	7.1531
767.1	8.12	4.60	3.421	675.0	300.0	767.1	3.421	0.7811	7.2508
747.1	8.13	4.61	3.423	675.0	300.0	747.1	3.423	0.7645	7.3458
727.1	8.14	4.61	3.424	675.0	300.0	727.1	3.424	0.7481	7.4382
707.1	8.14	4.61	3.425	675.0	300.0	707.1	3.425	0.7320	7.5280
687.1	8.15	4.61	3.427	675.0	300.0	687.1	3.427	0.7160	7.6150
667.1	8.16	4.62	3.428	675.0	300.0	667.1	3.428	0.7004	7.6992
647.1	8.16	4.62	3.429	675.0	300.0	647.1	3.429	0.6850	7.7808
627.1	8.17	4.62	3.430	675.0	300.0	627.1	3.430	0.6700	7.8595
607.1	8.18	4.62	3.431	675.0	300.0	607.1	3.431	0.6554	7.9354
587.1	8.18	4.62	3.433	675.0	300.0	587.1	3.433	0.6413	8.0085
567.1	8.19	4.63	3.434	675.0	300.0	567.1	3.434	0.6277	8.0786
547.1	8.19	4.63	3.435	675.0	300.0	547.1	3.435	0.6147	8.1458
527.1	8.20	4.63	3.436	675.0	300.0	527.1	3.436	0.6024	8.2100
507.1	8.20	4.63	3.437	675.0	300.0	507.1	3.437	0.5909	8.2711
487.1	8.21	4.63	3.438	675.0	300.0	487.1	3.438	0.5804	8.3291
467.1	8.21	4.63	3.438	675.0	300.0	467.1	3.438	0.5710	8.3839
447.1	8.22	4.63	3.439	675.0	300.0	447.1	3.439	0.5629	8.4353
427.1	8.22	4.64	3.440	675.0	300.0	427.1	3.440	0.5564	8.4834

Table 6 (*continued*)

Radius (in km)	V_P (in km/s)	V_S (in km/s)	Density (in kg/cm³)	Q_P	Q_S	Radius (in km)	Density (in kg/cm³)	Gravity (m/s²)	Pressure (in GPa)
407.1	8.23	4.64	3.441	675.0	300.0	407.1	3.441	0.5518	8.5279
387.1	8.23	4.64	3.442	675.0	300.0	387.1	3.442	0.5495	8.5687
380.0	8.23	4.64	3.442	675.0	300.0	380.0	3.442	0.5494	8.5823
380.0	?	0.0?	5.171	10000.0	10000.0	380.0	5.171	0.5494	8.5823
0.0	?	?	5.171	10000.0	10000.0	0.0	5.171	0.0000	9.6618

et al., 2006) and its size is not constrained by this study, the interpretation of the average core density into core composition is strongly limited.

6. Description of the best model

This section gives seismic event location parameters, station corrections, and the reference model. The reference model is denominated VPREMOON for Very Preliminary REference MOON model. The parameter values, and related error bars at fixed core radius, for this model are: $\rho_c = 2.762 \pm 0.0048$, $a = -8.0783 \pm 0.790$, $b = 4.728376 \pm 0.245$, $A = 1.816595 \pm 0.313$, $B = -0.000054 \pm 0.000251$ km^{-1} and $R_{core} = 380$ km. In this model, calculated values of geodesic observations are $k_2^{calc} = 0.0223$, $h_2^{calc} = 0.0394$, $IR^{calc} = 0.3932$ and $l_2^{calc} = 0.0106$ (this last parameter is not inverted here). The values obtained at best fit are $\chi^2_{seismo} = 1.4814$ and $\chi^2_{geod} = 0.0575$. For comparison, our starting model derived from Gagnepain-Beyneix et al. (2006) model gives $k_2^{calc} = 0.0231$, $h_2^{calc} = 0.0408$, $IR^{calc} = 0.3931$, $l_2^{calc} = 0.0110$, $\chi^2_{seismo} = 6.232$ and $\chi^2_{geod} = 0.301$.

Table 4 provides the relocations of the events used in this study inside the VPREMOON model. These locations are close to the locations published by Gagnepain-Beyneix et al. (2006) because the seismic model is very similar in most of the mantle. The errors on these locations are underestimated, because the uncertainty on the velocity model is not formally taken into account in their computation. Table 5 gives station corrections. These corrections are small and their relative error is large. Table 6 and Fig. 19 present the VPREMOON model. The model is separated in a seismic model in which the crustal thickness (28 km) is compatible with near side crustal structure below the Apollo network, and a geodesic model in which the Moho depth is corrected to its average value over the whole planet (40 km). P wave velocity inside the core is not constrained by our study. Assuming that the average core density is similar to the density of the liquid core, high pressure experiments suggest a P wave velocity close to 4.3 km/s at these pressure/temperature conditions (Sanloup et al., 2004). However, this value is not used in our model because the core internal structure is not constrained. P and S wave attenuations are taken from studies by Nakamura and Koyama (1982), Nakamura et al. (1982), and arbitrarily fixed in the deep mantle.

7. Conclusion

We have constructed a preliminary reference model of the Moon based on a priori crustal structure, physical constraints on density and seismic velocities variations with depth, by fitting both seismological and geodesic data. The core radius is determined from the detection of transversely polarized core reflected S wave from a low number of deep moonquakes properly located and presenting high signal to noise ratio. The VPREMOON model constrains the core size to 380 ± 40 km radius and average density to 5.2 ± 1.0 kg/cm³, and favours a liquid outer core. It constitutes the first reference model including simultaneously physical constraints, geodesic and seismological observations, and detection

of S waves reflected on the lunar core. However, the internal structure of the lunar core remains largely unknown, and the model is still characterized by rather strong uncertainties on the different parameters owing to the paucity of available data.

The constraints on the core density are strongly related to geodesic parameters such as the polar moment of inertia of the Moon, but also to the average crustal structure. The average crustal thickness is fixed in our model, but its variation can change significantly the polar moment of inertia budget of the planet, and consequently the core density obtained. Further constraints brought by SELENE and GRAIL missions on these parameters will indirectly strongly constrain the average core density, and the radius of the inner core which is expected for thermodynamical reasons (Wieczorek et al., 2006), and for which a seismic signature has been suggested by Weber et al. (2011). Our model relies on the hypotheses of homogeneity and adiabaticity of the lunar mantle. Consequently, radial and lateral deviations from this model, that may eventually be detected by future lunar seismometers, will provide additional constraints on the internal dynamics of the lunar interior. In particular, a high temperature gradient or partial melt inside the upper and lower boundary layers of the mantle may strongly modify seismic velocities and density in these regions. Both the very broad band planetary seismometers developed in the last decades (Lognonné et al., 1996, 2000, 2005) and future lunar geophysical stations, such as SELENE2 (Tanaka et al., 2008) and Lunette/ILN (Neal et al., 2010) will provide crucial additional data to further improve our knowledge of the lunar interior.

References

Alterman, Z., Jarosch, H., Pekeris, C.L., 1959. Oscillations of the Earth. Roy. Soc. Lond. Proc. Ser. A 252, 80–95.
Araki, H., 2001. Focal processes of deep moonquakes. J. Geod. Soc. Jpn. 47, 508–513.
Balog, P.S., Secco, R.A., Rubie, D.C., Frost, D.J., 2003. Equation of state of liquid Fe-10 wt% S: implications for the metallic cores of planetary bodies. J. Geophys. Res. (Solid Earth) 108, 2124–+.
Benz, W., Cameron, A.G.W., Melosh, H.J., 1989. The origin of the Moon and the single impact hypothesis. III. Icarus 81, 113–131.
Bina, C.R., 2003. Seismological constraints upon mantle composition. Treatise Geochem. 2, 39–59.
Birch, F., 1964. Density and composition of mantle and core. J. Geophys. Res. 69, 4377–4388.
Buland, R., Chapman, C., 1983. The computation of seismic travel times. Bull. Seismol. Soc. Am. 73, 1271–1301.
Calvet, M., Chevrot, S., 2005. Traveltime sensitivity kernels for PKP phases in the mantle. Phys. Earth Planet. Inter. 153, 21–31.
Canup, R.M., Asphaug, E., 2001. Origin of the Moon in a giant impact near the end of the Earth's formation. Nature 412, 708–712.

Chenet, H., Lognonné, P., Wieczorek, M., Mizutani, H., 2006. Lateral variations of lunar crustal thickness from the Apollo seismic data set. Earth Planet. Sci. Lett. 243, 1–14.

Cheng, C.H., Toksoz, M.N., 1978. Tidal stresses in the Moon. J. Geophys. Res. 83, 845–853.

Chevrot, S., 2002. Optimal waveform and delay time analysis by simulated annealing. Geophys. J. Int. 151, 164–171.

Dziewonski, A., Anderson, D., 1981. Preliminary reference Earth model. Phys. Earth Planet. Inter. 25, 297–356.

Efron, B., Tibshirani, R., 1993. An introduction to the bootstrap. CRC Press, monographs on Statistics and Applied Probability Series.

Gagnepain-Beyneix, J., Lognonné, P., Chenet, H., Lombardi, D., Spohn, T., 2006. A seismic model of the lunar mantle and constraints on temperature and mineralogy. Phys. Earth Planet. Inter. 159, 140–166.

Goossens, S., Matsumoto, K., 2008. Lunar degree 2 potential Love number determination from satellite tracking data. GRL 35, 2204–+.

Hood, L.L., Jones, J.H., 1987. Geophysical constraints on lunar bulk composition and structure – a reassessment. J. Geophys. Res. 92, 396–+.

Hood, L.L., Mitchell, D.L., Lin, R.P., Acuna, M.H., Binder, A.B., 1999. Initial measurements of the lunar induced magnetic dipole moment using lunar prospector magnetometer data. Geophys. Res. Lett. 26, 2327–2330.

Kennett, B., Engdahl, E., 1991. Traveltimes for global earthquake location and phase identification. Geophys. J. Int. 105, 429–465.

Khan, A., Connolly, J.A.D., Maclennan, J., Mosegaard, K., 2007. Joint inversion of seismic and gravity data for lunar composition and thermal state. Geophys. J. Int. 168, 243–258.

Khan, A., Mosegaard, K., 2002. An inquiry into the lunar interior: a nonlinear inversion of the Apollo lunar seismic data. J. Geophys. Res. (Planets) 107, 5036–+.

Khan, A., Mosegaard, K., 2005. Further constraints on the deep lunar interior. Geophys. Res. Lett. 32, 22203–+.

Khan, A., Mosegaard, K., Williams, J.G., Lognonné, P., 2004. Does the Moon possess a molten core? Probing the deep lunar interior using results from LLR and lunar prospector. J. Geophys. Res. (Planets) 109, 9007–+.

Konopliv, A.S., Asmar, S.W., Carranza, E., Sjogren, W.L., Yuan, D.N., 2001. Recent gravity models as a result of the lunar prospector mission. Icarus 150, 1–18.

Koyama, J., Nakamura, Y., 1980. Focal mechanism of deep moonquakes. In: Bedini, S.A. (Ed.), Lunar and Planetary Science Conference Proceedings, vol. 11 of Lunar and Planetary Science Conference Proceedings, pp. 1855–1865.

Kuskov, O.L., Kronrod, V.A., 1998. Constitution of the Moon5. Constraints on composition, density, temperature, and radius of a core. Phys. Earth Planet. Inter. 107, 285–306.

Kuskov, O.L., Kronrod, V.A., Hood, L.L., 2002. Geochemical constraints on the seismic properties of the lunar mantle. In: Lunar and Planetary Institute Science Conference Abstracts, vol. 33 of Lunar and Planetary Institute Science Conference Abstracts, pp. 1501–+.

Larose, E., Khan, A., Nakamura, Y., Campillo, M., 2005. Lunar subsurface investigated from correlation of seismic noise. Geophys. Res. Lett. 32, 16201–+.

Lognonné, P., 2005. Planetary seismology. Ann. Rev. Earth Planet. Sci. 33, 19.1–19.34.

Lognonné, P., Beyneix, J.G., Banerdt, W.B., Cacho, S., Karczewski, J.F., Morand, M., 1996. Ultra broad band seismology on InterMarsNet. Planet. Space Sci. 44, 1237–1249.

Lognonné, P., Gagnepain-Beyneix, J., Chenet, H., 2003. A new seismic model of the Moon: implications for structure, thermal evolution and formation of the Moon. Earth Planet. Sci. Lett. 211, 27–44.

Lognonné, P., Giardini, D., Banerdt, B., Gagnepain-Beyneix, J., Mocquet, A., Spohn, T., Karczewski, J.F., Schibler, P., Cacho, S., Pike, W.T., Cavoit, C., Desautez, A., Favède, M., Gabsi, T., Simoulin, L., Striebig, N., Campillo, M., Deschamp, A., Hinderer, J., Lévéque, J.J., Montagner, J.P., Rivéra, L., Benz, W., Breuer, D., Defraigne, P., Dehant, V., Fujimura, A., Mizutani, H., Oberst, J., 2000. The NetLander very broad band seismometer. Planet. Space Sci. 48, 1289–1302.

Lognonné, P., Johnson, C., 2007. Planetary seismology. Treatise Geophys. 10, 69–122.

Margerin, L., Campillo, M., van Tiggelen, B.A., Hennino, R., 2009. Energy partition of seismic coda waves in layered media: theory and application to Pinyon flats observatory. Geophys. J. Int. 177, 571–585.

Mueller, S., Taylor, G.J., Phillips, R.J., 1988. Lunar composition – a geophysical and petrological synthesis. J. Geophys. Res. 93, 6338–6352.

Nakamura, Y., 1978. A1 moonquakes – source distribution and mechanism. In: Lunar and Planetary Science Conference Proceedings, vol. 9 of Lunar and Planetary Science Conference Proceedings, pp. 3589–3607.

Nakamura, Y., 1983. Seismic velocity structure of the lunar mantle. J. Geophys. Res. 88, 677–686.

Nakamura, Y., Duennebier, F.K., Latham, G.V., Dorman, H.J., 1976. Structure of the lunar mantle. J. Geophys. Res. 81, 4818–4824.

Nakamura, Y., Koyama, J., 1982. Seismic Q of the lunar upper mantle. J. Geophys. Res. 87, 4855–4861.

Nakamura, Y., Latham, G.V., Dorman, H.J., 1982. Apollo lunar seismic experiment – final summary. In: Boynton, W.V., Ahrens, T.J. (Eds.), Lunar and Planetary Science Conference Proceedings, vol. 13 of Lunar and Planetary Science Conference Proceedings, pp. 117–+.

Neal, C.R., Banerdt, W.B., Alkalai, L., 2010. LUNETTE: establishing a lunar geophysical network without nuclear power through a discovery-class mission. In: Lunar and Planetary Institute Science Conference Abstracts, vol. 41 of Lunar and Planetary Institute Science Conference Abstracts, pp. 2710–+.

Neidell, N.S., Taner, T.M., 1971. Semblance and other coherency measures for multichannel data. Geophysics 36, 482–497.

Nuttli, O., 1961. The effect of the Earth's surface on the S wave particle motion. Bull. Seismol. Soc. Am. 51, 237–246.

Oldham, R.D., 1914. The constitution of the interior of the Earth as revealed by earthquakes. Nature 92, 684–685.

Russell, C.T., Coleman Jr., P.J., Goldstein, B.E., 1982. Measurements of the lunar induced magnetic moment in the geomagnetic tail – evidence for a lunar core. In: Merrill, R.B., Ridings, R. (Eds.), Lunar and Planetary Science Conference Proceedings, vol. 12 of Lunar and Planetary Science Conference Proceedings, pp. 831–836.

Sambridge, M., 1999. Geophysical inversion with a neighbourhood algorithm-I. Searching a parameter space. Geophys. J. Int. 138, 479–494.

Sanloup, C., Fiquet, G., Gregoryanz, E., Morard, G., Mezouar, M., 2004. Effect of Si on liquid Fe compressibility: implications for sound velocity in core materials. Geophys. Res. Lett. 31, 7604–+.

Sanloup, C., Guyot, F., Gillet, P., Fiquet, G., Mezouar, M., Martinez, I., 2000. Density measurements of liquid Fe-S alloys at high-pressure. Geophys. Res. Lett. 27, 811–814.

Sens-Schönfelder, C., Larose, E., 2008. Temporal changes in the lunar soil from correlation of diffuse vibrations. Phys. Rev. E 78 (4), 045601–+.

Tanaka, S., Shiraishi, H., Kato, M., Okada, T., group of Post SELENE missions, S.W., 2008. The science objectives of the SELENE-II mission as the post SELENE mission. Adv. Space Res. 42, 394–401.

Tarantola, A., 1987. Inverse Problem Theory. Elsevier Science Publishers, B.V., Amsterdam.

Toksoz, M.N., Dainty, A.M., Solomon, S.C., Anderson, K.R., 1974. Structure of the Moon. Rev. Geophys. Space Phys. 12, 539–567.

Vinnik, L., Chenet, H., Gagnepain-Beyneix, J., Lognonne, P., 2001. First seismic receiver functions on the Moon. Geophys. Res. Lett. 28, 3031–3034.

von Rebeur-Paschwitz, E., 1889. The Earthquake of Tokio, April 18, 1889. Nature 40, 294–295.

Weber, R.C., Bills, B.G., Johnson, C.L., 2009. Constraints on deep moonquake focal mechanisms through analyses of tidal stress. J. Geophys. Res. (Planets) 114, 5001–+.

Weber, R.C., Lin, P., Garnero, E.J., Williams, Q., Lognonné, P., 2011. Seismic detection of the lunar core. Science 331, 309–.

Wieczorek, M., Jolliff, B., Khan, A., Pritchard, M., Weiss, B., Williams, J., Hood, L., Righter, K., Neal, C., Shearer, C., McCallum, I., Tompkins, S., Hawke, B., Peterson, C., Gillis, J., Bussey, B., 2006. The constitution and structure of the lunar interior. Rev. Min. Geochem. 60, 221–364.

Williams, J.G., 2007. A scheme for lunar inner core detection. Geophys. Res. Lett. 34, 3202–+.

Williams, J.G., Boggs, D.H., Yoder, C.F., Ratcliff, J.T., Dickey, J.O., 2001. Lunar rotational dissipation in solid body and molten core. J. Geophys. Res. 106, 27933–27968.

Update

Physics of the Earth and Planetary Interiors

Contents lists available at SciVerse ScienceDirect

Physics of the Earth and Planetary Interiors

journal homepage: www.elsevier.com/locate/pepi

Erratum

Erratum to "Very Preliminary Reference Moon Model", by R.F. Garcia, J. Gagnepain-Beyneix, S. Chevrot, P. Lognonné [Phys. Earth Planet. Inter. 188 (2011) 96–113]

Raphaël F. Garcia [a,b,*], Jeannine Gagnepain-Beyneix [c], Sébastien Chevrot [a,b], Philippe Lognonné [c]

[a] Université de Toulouse, UPS-OMP, IRAP, Toulouse, France
[b] CNRS, IRAP, 14, Avenue Edouard Belin, F-31400 Toulouse, France
[c] Equipe Géophysique Spatiale et Planétaire, Institut de Physique du Globe, Sorbonne Paris Cité, Univ Paris Diderot, UMR 7154 CNRS,
4 Ave de Neptune F-94100 Saint Maur des Fossés, France

After publication of this paper we noticed some mistakes in the a priori deep moonquake locations used for waveform data analysis (Table 2), and an error in the final computation of pressure inside the Moon (Table 6 and Fig. 19).

The locations given in Table 2 are not exactly similar to the ones given in Gagnepain-Beyneix et al. (2006), due to a data

reprocessing of some events after publication of the 2006 paper. The latitude of event A10 is opposite to the one given in Table 2 of the paper, and recent studies suggest that this event cluster is identical to A24 event cluster (Y. Nakamura, personal communication). However, this error does not affect the results because this event is not used for the inversion of mantle structure

Table 6
VPREMOON model: on the left the seismic model and on the right the geodesic model in which Moho depth as been corrected to 40 km. Attenuation parameters are extracted from previous studies (Nakamura and Koyama, 1982; Nakamura et al., 1982) and arbitrarily fixed in the deep mantle. Seismic velocities and attenuation parameters inside the core are arbitrarily fixed by the authors.

Radius (in km)	V_P (in km/s)	V_S (in km/s)	Density (in kg/cm^3)	Q_P	Q_S	Radius (in km)	Density (in kg/cm^3)	Gravity (m/s^2)	Pressure (in GPa)
1737.1	1.00	0.50	2.600	6750.0	6750.0	1737.1	2.600	1.6248	0.0000
1736.1	1.00	0.50	2.600	6750.0	6750.0	1736.1	2.600	1.6245	0.0042
1736.1	3.20	1.80	2.762	6750.0	6750.0	1736.1	2.762	1.6245	0.0042
1725.1	3.20	1.80	2.762	6750.0	6750.0	1725.1	2.762	1.6196	0.0535
1725.1	5.50	3.30	2.762	6750.0	6750.0	1725.1	2.762	1.6196	0.0535
1709.1	5.50	3.30	2.762	6750.0	6750.0	1709.1	2.762	1.6127	0.1249
1709.1	7.54	4.34	3.312	6750.0	6750.0	1697.1	2.762	1.6076	0.1783
1697.1	7.55	4.34	3.314	6750.0	6750.0	1697.1	3.314	1.6076	0.1783
1671.7	7.57	4.35	3.318	9000.0	4000.0	1671.7	3.318	1.5851	0.3127
1647.1	7.59	4.36	3.322	9000.0	4000.0	1647.1	3.322	1.5632	0.4413
1627.1	7.61	4.37	3.325	9000.0	4000.0	1627.1	3.325	1.5454	0.5446
1607.1	7.63	4.38	3.329	9000.0	4000.0	1607.1	3.329	1.5276	0.6469
1587.1	7.64	4.39	3.332	9000.0	4000.0	1587.1	3.332	1.5098	0.7480
1567.1	7.66	4.40	3.335	9000.0	4000.0	1567.1	3.335	1.4920	0.8481
1547.1	7.68	4.40	3.338	9000.0	4000.0	1547.1	3.338	1.4741	0.9470
1527.1	7.69	4.41	3.341	9000.0	4000.0	1527.1	3.341	1.4562	1.0449
1502.0	7.71	4.42	3.344	9000.0	4000.0	1502.0	3.344	1.4338	1.1661
1487.1	7.72	4.43	3.346	9000.0	4000.0	1487.1	3.346	1.4204	1.2373
1461.7	7.74	4.44	3.350	3375.0	1500.0	1461.7	3.350	1.3976	1.3571
1447.1	7.75	4.44	3.352	3375.0	1500.0	1447.1	3.352	1.3845	1.4251
1427.1	7.77	4.45	3.355	3375.0	1500.0	1427.1	3.355	1.3666	1.5174
1407.1	7.78	4.45	3.357	3375.0	1500.0	1407.1	3.357	1.3486	1.6085
1387.1	7.80	4.46	3.360	3375.0	1500.0	1387.1	3.360	1.3306	1.6985
1367.1	7.81	4.47	3.363	3375.0	1500.0	1367.1	3.363	1.3126	1.7874
1347.1	7.82	4.47	3.365	3375.0	1500.0	1347.1	3.365	1.2946	1.8751

DOI of original article: http://dx.doi.org/10.1016/j.pepi.2011.06.015
* Corresponding author at: Université de Toulouse, UPS-OMP, IRAP, Toulouse, France. Tel.: +33 5 61 33 30 45; fax: +33 5 61 33 29 00.
  E-mail address: garcia@dtp.obs-mip.fr (R.F. Garcia).

Table 6 (*continued*)

Radius (in km)	V_P (in km/s)	V_S (in km/s)	Density (in kg/cm³)	Q_P	Q_S	Radius (in km)	Density (in kg/cm³)	Gravity (m/s²)	Pressure (in GPa)
1327.1	7.84	4.48	3.368	3375.0	1500.0	1327.1	3.368	1.2766	1.9616
1307.1	7.85	4.49	3.370	3375.0	1500.0	1307.1	3.370	1.2586	2.0470
1287.1	7.86	4.49	3.373	3375.0	1500.0	1287.1	3.373	1.2405	2.1313
1267.1	7.88	4.50	3.375	3375.0	1500.0	1267.1	3.375	1.2225	2.2144
1252.0	7.88	4.50	3.377	3375.0	1500.0	1252.0	3.377	1.2089	2.2764
1231.7	7.90	4.51	3.379	1125.0	500.0	1231.7	3.379	1.1906	2.3586
1207.1	7.91	4.51	3.382	1125.0	500.0	1207.1	3.382	1.1685	2.4567
1187.1	7.92	4.52	3.384	1125.0	500.0	1187.1	3.384	1.1505	2.5352
1167.1	7.94	4.53	3.386	1125.0	500.0	1167.1	3.386	1.1325	2.6125
1147.1	7.95	4.53	3.388	1125.0	500.0	1147.1	3.388	1.1145	2.6886
1127.1	7.96	4.54	3.391	1125.0	500.0	1127.1	3.391	1.0965	2.7635
1107.1	7.97	4.54	3.393	1125.0	500.0	1107.1	3.393	1.0786	2.8373
1087.1	7.98	4.54	3.395	1125.0	500.0	1087.1	3.395	1.0606	2.9099
1067.1	7.99	4.55	3.397	1125.0	500.0	1067.1	3.397	1.0427	2.9813
1047.1	8.00	4.55	3.398	1125.0	500.0	1047.1	3.398	1.0249	3.0515
1027.1	8.01	4.56	3.400	1125.0	500.0	1027.1	3.400	1.0070	3.1206
1002.0	8.02	4.56	3.403	1125.0	500.0	1002.0	3.403	0.9847	3.2056
987.1	8.03	4.57	3.404	1125.0	500.0	987.1	3.404	0.9715	3.2552
961.7	8.04	4.57	3.406	675.0	300.0	961.7	3.406	0.9490	3.3383
947.1	8.05	4.57	3.408	675.0	300.0	947.1	3.408	0.9361	3.3852
927.1	8.06	4.58	3.409	675.0	300.0	927.1	3.409	0.9185	3.4484
907.1	8.07	4.58	3.411	675.0	300.0	907.1	3.411	0.9010	3.5104
887.1	8.08	4.58	3.413	675.0	300.0	887.1	3.413	0.8835	3.5713
867.1	8.08	4.59	3.414	675.0	300.0	867.1	3.414	0.8662	3.6310
847.1	8.09	4.59	3.416	675.0	300.0	847.1	3.416	0.8489	3.6896
827.1	8.10	4.59	3.417	675.0	300.0	827.1	3.417	0.8318	3.7470
807.1	8.11	4.60	3.419	675.0	300.0	807.1	3.419	0.8147	3.8033
787.1	8.12	4.60	3.420	675.0	300.0	787.1	3.420	0.7978	3.8584
767.1	8.12	4.60	3.421	675.0	300.0	767.1	3.421	0.7811	3.9124
747.1	8.13	4.61	3.423	675.0	300.0	747.1	3.423	0.7645	3.9653
727.1	8.14	4.61	3.424	675.0	300.0	727.1	3.424	0.7481	4.0171
707.1	8.14	4.61	3.425	675.0	300.0	707.1	3.425	0.7320	4.0678
687.1	8.15	4.61	3.427	675.0	300.0	687.1	3.427	0.7160	4.1174
667.1	8.16	4.62	3.428	675.0	300.0	667.1	3.428	0.7004	4.1660
647.1	8.16	4.62	3.429	675.0	300.0	647.1	3.429	0.6850	4.2135
627.1	8.17	4.62	3.430	675.0	300.0	627.1	3.430	0.6700	4.2599
607.1	8.18	4.62	3.431	675.0	300.0	607.1	3.431	0.6554	4.3054
587.1	8.18	4.62	3.433	675.0	300.0	587.1	3.433	0.6413	4.3499
567.1	8.19	4.63	3.434	675.0	300.0	567.1	3.434	0.6277	4.3935
547.1	8.19	4.63	3.435	675.0	300.0	547.1	3.435	0.6147	4.4361
527.1	8.20	4.63	3.436	675.0	300.0	527.1	3.436	0.6024	4.4780
507.1	8.20	4.63	3.437	675.0	300.0	507.1	3.437	0.5909	4.5190
487.1	8.21	4.63	3.438	675.0	300.0	487.1	3.438	0.5804	4.5592
467.1	8.21	4.63	3.438	675.0	300.0	467.1	3.438	0.5710	4.5988
447.1	8.22	4.63	3.439	675.0	300.0	447.1	3.439	0.5629	4.6378
427.1	8.22	4.64	3.440	675.0	300.0	427.1	3.440	0.5564	4.6763
407.1	8.23	4.64	3.441	675.0	300.0	407.1	3.441	0.5518	4.7144
387.1	8.23	4.64	3.442	675.0	300.0	387.1	3.442	0.5495	4.7523
380.0	8.23	4.64	3.442	675.0	300.0	380.0	3.442	0.5494	4.7657
380.0	?	0.00?	5.171	10000.0	10000.0	380.0	5.171	0.5494	4.7657
0.0	?	?	5.171	10000.0	10000.0	0.0	5.171	0.0000	5.3055
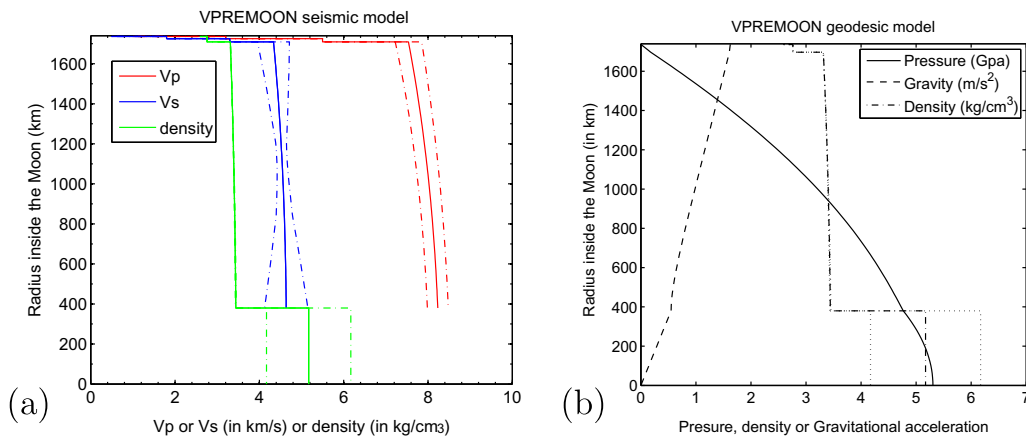
Fig. 19. VPREMOON seismological (a) and geodesic models (b). On the left (a), P and S wave velocities (in km/s) and density (in kg/cm³) are plotted as a function of radius (in km) for the seismological model. The error bars are indicated for each parameters by dot-dashed lines. On the right (b), pressure (in GPa), gravity (in m/s²) and density (in kg/cm³) are plotted as a function of radius (in km) for the geodesic model.

(see Table 4 of the original paper), and also not used for core reflected phase detection.

A mistake was detected in the computation of the pressure inside the Moon from density and gravity models (M. Wieczoreck, personal communication). This error does not modify the rest of the results, but correct values for Table 6 and Fig. 19 are reproduced below.

We thank the editors for the opportunity to make this correction.

Reference

Gagnepain-Beyneix, J., Lognonné, P., Chenet, H., Lombardi, D., Spohn, T., 2006. A seismic model of the lunar mantle and constraints on temperature and mineralogy. Phys. Earth Planet. Inter. 159, 140–166.